Chapter 12 REMOTE SENSING OF SEA STATE BY RADAR

Donald E. Barrick
Electromagnetics Division
Battelle, Columbus Laboratories

Several radar techniques have evolved over recent years which permit the straightforward measurement of certain important ocean wave parameters. At MF and HF, the ocean waveheight spatial spectrum can be measured directly via the first-order Bragg-scattered signal intensity; a variety of experiments are briefly examined which involve monostatic ground-wave and ionospheric radars, bistatic HF buoy-shore systems, bistatic LORAN A signal scatter systems, and bistatic buoy-satellite systems. The second-order contributions to HF scatter produce a continuous Doppler return which varies in position and amplitude with sea state. At UHF, it is possible to measure indirectly the spatial slope spectrum of the longer ocean waves via cross-correlation of simultaneous Bragg-effect returns at two frequencies. Finally, short-pulse microwave satellite altimeters permit a direct measurement of the significant (or rms) waveheight of the sea at the suborbital point via the specular point scatter mechanism. These techniques will be important for (i) detailed oceanographic measurements of the characteristics of sea waves, (ii) routine monitoring of sea state for maritime purposes, and (iii) deduction of wind patterns above the seas for meteorological purposes.

12.1 Description of the Sea Surface

The quantitative interpretation of radar scatter from the sea requires the use and appreciation of certain properties of ocean waves. A brief review is undertaken here of the ocean-wave physics and characteristics which we will need later; also, common oceanographic nomenclature pertaining to ocean waves is defined and explained. A readable but detailed treatment of all aspects of ocean wave physics can be found in the text by Kinsman (1965); a more elementary introduction to water waves is the concise soft-cover booklet by Bascom (1964).

12.1.1 Nomenclautre

Sea State. This term as used here refers to the state of the sea, or roughness, as determined by the heights of the largest waves present. Numbers have been assigned to sea states by the International Mariners' Codes, and these are related to wave heights in (T12.1).

Significant Wave Height. This term is a common maritime descriptor referring to the average of the heights—*from crest to trough*—of the 1/3 highest waves; it is denoted $H_{1/3}$.

RMS Wave (or Roughness) Height. This is a term describing root-mean-square height—*above the mean surface level*—used in rough surface scatter theories; it is denoted here by h. While there is no exact general relationship between h and $H_{1/3}$, a common approximation frequently used for wind waves is $H_{1/3} \simeq 2.83$ h.

Length. The length or spatial period of a single ocean wave is the distance from one crest to another; it is denoted L.

Period. Unless denoted otherwise, this refers to the temporal period, and is the length of time it takes two successive crests of a single wave to pass one point. It is denoted T.

Spatial Wavenumber. This is defined in terms of the length of an ocean wave as $\kappa = 2\pi/L$.

Temporal Wavenumber. This radian wavenumber is given in terms of the period by $\omega = 2\pi/T$.

Fetch. The fetch is the horizontal distance over which a nearly constant wind has been blowing.

Duration. This term refers to the length of time during which a nearly constant wind has been blowing.

Wind Waves. This term refers to a system of ocean waves which is being, or has very recently been, aroused by winds blowing locally above that area of the ocean. Wind waves result in a random appearing ocean height profile.

Fully Developed Seas. This is an equilibrium sea state condition reached after sufficient duration and fetch at a given wind speed. The estimated duration and fetch versus wind speed required to produce fully developed seas is provided in (T12.1)

Table 12.1 Deep-Water Wind Waves And Sea State

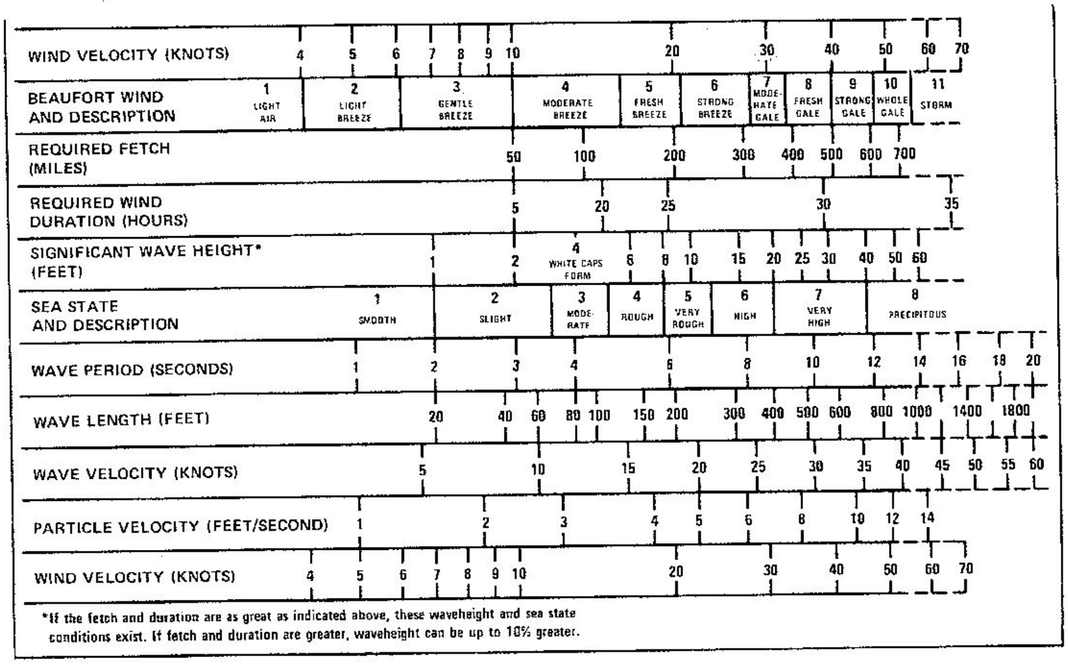

*If the fetch and duration are as great as indicated above, these waveheight and sea state conditions exist. If fetch and duration are greater, waveheight can be up to 10% greater.

Swell. When wind waves move out of the area in which they were originally excited by the winds, or after winds have ceased to blow, these waves change their shape and settle down to what is known as "swell". Swell appears less random and more nearly sinusoidal, of great length, and with great width along the crestlines. The usual period of swell is from six to sixteen seconds. Swell, while an occasional phenomenon, can arise from storm areas thousands of miles distant.

Deep-Water Waves. When the water is sufficiently deep that the effect of the bottom on the propagation characteristics of the waves can be neglected, they are called "deep-water" waves. Generally, if the depth is greater than 1/2 the length of a given wave, the deep-water approximation is valid. Except near beaches, ocean waves are deep-water waves, and we utilize this assumption throughout this chapter.

Gravity Waves. This term refers to waves in which the chief restoring force upon the perturbed water mass is gravity. Waves whose lengths, L, are greater than 1.73 cm (Phillips, 1966) are gravity waves. Since gravity waves are the essence of sea state, they are the only types of waves considered in this chapter.

Capillary Waves. This term refers to waves in which the chief restoring force acting on the perturbed water mass is surface tension. Less than 1.73 cm in length, they are not important for most of the topics of this chapter.

12.1.2 Wind Wave Surface Height and Slope Distributions

Patterns of wind waves having various lengths, heights, and directions of motion interact to form a random-appearing surface. Hence the quantitative characteristics of such a surface are best described statistically. One of the statistical functions frequently occurring in the analysis of radio wave interactions with the sea is the probability density function of the surface height and its spatial derivatives (or slopes). Physically, the probability density function p(x) is defined such that p(x)dx is the probability that the random variable lies in the interval dx between x – dx/2 and x + dx/2.

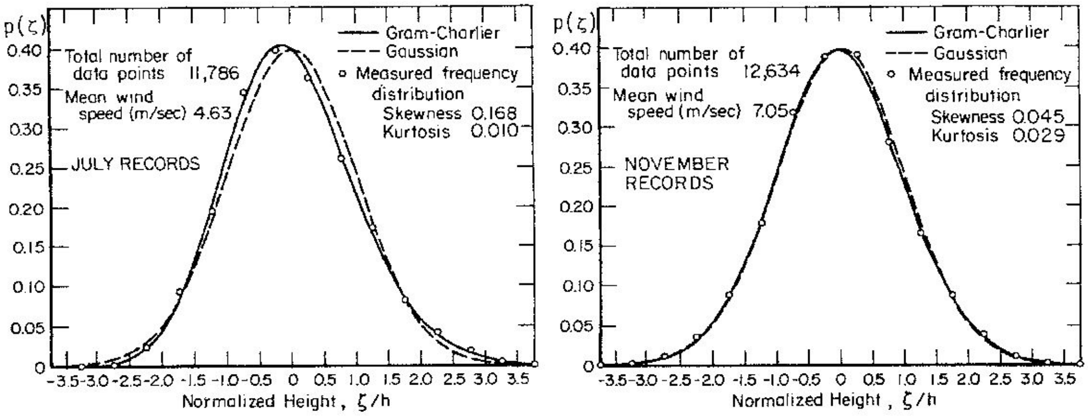

Figure 12.1 *Measured versus model probability density functions for sea surface height (after MacKay, 1959).*

For the sea surface height, ζ, above the mean sea level, MacKay (1959) found from detailed analyses of measured wave records that the height probability density function is nearly Gaussian (or normal). This yields

$$p(\zeta) = (2\pi h^2)^{-1/2} \exp\left\{-\frac{\zeta^2}{2h^2}\right\} \qquad (12:1)$$

where h is the rms height of the surface, i.e., $h = (\langle\zeta^2\rangle)^{1/2}$, where $\langle \ldots \rangle$ denotes average. The actual density for the sea height cannot be truly Gaussian for two reasons: (i) For Gaussian distributed waves, there is always some finite—albeit small—probability that very large waveheights can occur, whereas for the sea, wave breaking occurs when the heights and slopes exceed certain critical values. (ii) The Gaussian function is symmetric, whereas the sea height is not truly symmetric about the mean. This can be seen from looking at the sea surface profile, which tends to have sharp pointed peaks (for $\zeta > 0$), but rounded shallow troughs (for $\zeta < 0$). Thus the sea surface profile would not look the same upside down, whereas a true Gaussian variable would.

For the latter reason, the true height probability density function is slightly better matched by a Gram-Charlier model than by the Gaussian, as shown in (F12.1), after MacKay (1959). The difference is very slight, however, and for most analytical purposes the Gaussian model is entirely adequate†. The Gaussian height distribution will be assumed and used throughout this chapter.

If the height distribution for the sea were truly Gaussian, then the distribution of its spatial derivatives (i.e., the slopes) would also be Gaussian, because a linear operation on a Gaussian random variable (e.g., differentiation) produces another Gaussian random variable. The actual slope distributions for the sea are again almost—but not quite—Gaussian. We take the x-axis as horizontal and pointing in the dominant wind direction (i.e., along the downwind direction), and the y-axis as horizontal and pointing in the crosswind direction. Then Cox and Munk (1954), using glitter point photography to measure the directional slopes, find that ζ_y $(= \partial\zeta/\partial y)$ in the crosswind direction is symmetric, but ζ_x $(= \partial\zeta/\partial x)$ is skewed toward the upwind direction, probably due to wind stress. This is shown in (F12.2). Thus the departure from Gaussian is again slight, and while it could be important in applications involving radar scatterometers looking near the vertical with high angular resolution (Nathanson, 1971), the difference is ignored in this chapter. Also noteworthy from the figures is the fact that the observed rms slope in the upwind-downwind direction is not significantly different from that in the crosswind direction. It can be shown analytically that ζ_x and ζ_y are uncorrelated at any given point on the ocean. Therefore, we take the following for the *joint* probability density function for the surface slopes:

$$p(\zeta_x,\zeta_y) = (\pi s^2)^{-1} \exp\left\{-\frac{\zeta_x^2 + \zeta_y^2}{s^2}\right\} \qquad (12:2)$$

---

† One case where one might desire a higher order correction to the Gaussian model accounting for the skewness is in a detailed analysis of the short pulse return from a radar altimeter.

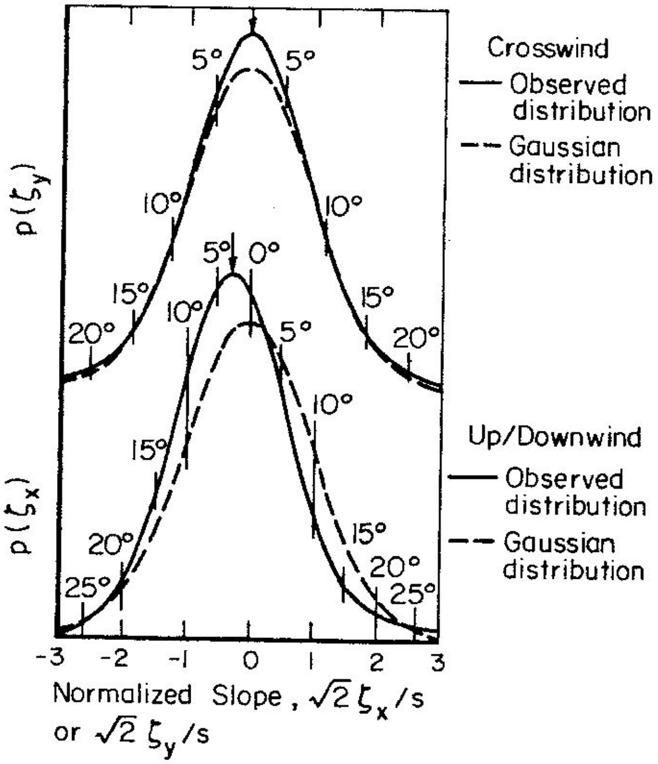

Figure 12.2 *Measured versus model probability density functions for sea surface slopes (after Cox and Munk, 1954).*

where, as explained above, we take $s^2 = \langle \zeta_x^2 + \zeta_y^2 \rangle = \langle \zeta_x^2 \rangle + \langle \zeta_y^2 \rangle = 2\langle \zeta_x^2 \rangle = 2\langle \zeta_y^2 \rangle$, s being the *total* rms slope of the ocean surface at a given point.

12.1.3 First-Order Gravity Wave Dispersion Relationship

The equation for the surface height, ζ, of a deep-water gravity wave is obtained from hydrodynamic theory (Kinsman, 1965). Generally, the wave surface height, ζ, is a function of the two orthogonal horizontal coordinates x,y and of time, t, i.e., $\zeta(x,y,t)$. This function—as well as the velocity potential and stream function—must satisfy Laplace's second-order differential equation; in addition, they satisfy two boundary conditions at the free surface: (i) the kinematic condition and (ii) the dynamic condition. While Laplace's differential equation is linear, the boundary conditions are not. Thus an exact solution is difficult to obtain.

The common method of solving these equations is to expand all of the functions into a perturbational series. Then the nonlinear boundary conditions are ordered into several equations, each containing terms of a higher order of magnitude. The ordering (or perturbational) parameter is the height of a wave divided by its length; this quantity is always very small for gravity waves. The lowest-order equations to emerge are linear and can be solved for the first-order height, ζ, of the surface. Second and higher-order solutions for ζ can also be obtained, and will be discussed in a later section. As the height of the water wave decreases, the first-order solution becomes increasingly valid because higher-order terms decrease in magnitude. Hence, the first-order solution is also referred to as the small-amplitude approximation for water waves.

The first-order solution, ζ, has several distinctive characteristics. It can consist of the superposition of an arbitrary number of sinusoids of different amplitudes, spatial lengths, and directions. *But*—unique to water waves—each sinusoid of a given wavelength (or wavenumber) moves at a distinct phase velocity. The relationship for the first-order phase velocity, v, is obtained also from the lowest-order surface boundary conditions. It is (for gravity waves)

$$v = \sqrt{\frac{gL}{(2\pi)}} = \sqrt{\frac{g}{\kappa}}\,, \qquad (12:3)$$

where g is the acceleration of gravity (≈ 9.81 m/s), and $\kappa = 2\pi/L$ is the total spatial wavenumber for the wave of length L.

Another way of stating (12:3) is to relate the temporal wavenumber, ω, of the wave to its spatial wavenumbers; this is commonly called a dispersion relationship in physics. It is

$$\omega^2 = g\kappa = g\sqrt{\kappa_x{}^2 + \kappa_y{}^2}\,, \qquad (12:4)$$

where we assume for generality that the wave is moving in a direction whose angle θ with respect to the x-axis is given by $\tan^{-1}(\kappa_y/\kappa_x)$. The total wavenumber magnitude, κ, is thus the square root of the sum of the squares of the x- and y-directed spatial wavenumbers κ_x and κ_y.

From (12:4) we can obtain still another commonly seen first-order expression relating the wavelength to the period:

$$T^2 = \left(\frac{2\pi}{g}\right)L\,. \qquad (12:5)$$

Table 12.2 Relationship Between Period, Length, And Phase Velocity Of Small Amplitude Gravity Waves

Period, T, seconds	Wave Length, L		Velocity, v	
	feet	meters	knots	meters/second
6	184	56	18.1	9.3
8	326	100	24.1	12.4
10	512	156	30.2	15.5
12	738	225	36.2	18.6
14	1000	305	42.4	21.8
16	1310	400	48.6	25.0

Thus we see for first-order gravity waves a unique square root relationship between the water wavelength and its temporal characteristics such as its velocity and period. Table (12.2) provides a ready connection between these quantities for the longer, higher waves which generally comprise sea state. It will be seen later that this square-root dispersion relationship forms the basis for several unique radar experiments involving scatter from sea waves.

12.1.4 Waveheight Spectrum of Wind Waves

The statistical quantity developed by oceanographers to relate the height of ocean waves to their length is the waveheight spectrum. It will be seen later that this spectrum also appears directly in radar scatter theories. The most general form for this spectrum contains two spatial wavenumbers (κ_x, κ_y) and one temporal wavenumber (ω) to describe the waveheight $\zeta(x,y,t)$ as a function of its three independent variables; we denote it as $S(\kappa_x, \kappa_y, \omega)$.

For a random-like system of wind waves, we assume that the dominant wind and wave direction is in the +x direction. Then we can express the surface height in a Fourier series as a sum of traveling waves:

$$\zeta = \sum_{m,n,k=-\infty}^{\infty} P(m,n,k)e^{iamx+iany-iwkt} = \sum_{m,n=-\infty}^{\infty} P(m,n)e^{ia(mx+ny)-i\omega_+ t}\,. \qquad (12:6)$$

Here $a = 2\pi/L_f$ and $w = 2\pi/T_f$, where L_f and T_f are the wavelength and period of the fundamental components in the expansion. The wavenumbers of each sinusoid are then $\kappa_x = am$, $\kappa_y = an$, $\omega = wk$. The first summation in (12:6) is more general, assuming no particular dispersion relationship. Because first-order water waves are constrained to follow the dispersion relationship expressed by (12:4), however, it is possible to simplify this to a double summation over two independent indices (or wavenumbers); the third is given in terms of the first two as

$$\omega_+ = \mathrm{sgn}(am)(ag)^{1/2}(m^2 + n^2)^{1/4} = \mathrm{sgn}(\kappa_x)g^{1/2}(\kappa_x{}^2 + \kappa_y{}^2)^{1/4} , \tag{12:7}$$

where $\mathrm{sgn}(u) = \pm 1$ depending upon whether its argument u is ±.

The first-order spatial/temporal average waveheight spectrum can now be written in terms of the Fourier coefficients of the expansion (Barrick, 1972):

$$\langle P(m,n,k)P(m',n',k')\rangle = \begin{cases} \dfrac{(2\pi)^3}{L_f^2 T_f}\, S(\kappa_x,\kappa_y,\omega) \text{ for} \begin{cases} m' = -m \\ n' = -n \\ k' = -k \end{cases} \\ \\ 0 \text{ for other } m',n',k' \end{cases} \tag{12:8}$$

and

$$\langle P(m,n)P(m',n')\rangle = \begin{cases} \left(\dfrac{2\pi}{L_f}\right)^2 S(\kappa_x,\kappa_y) \text{ for} \begin{cases} m' = -m \\ n' = -n \end{cases} \\ \\ 0 \text{ for other } m',\, n' \end{cases} \tag{12:9}$$

Again, using the first-order dispersion relationships it is possible to express the more general $S(\kappa_x,\kappa_y,\omega)$ in terms of the directional spatial spectrum, $S(\kappa_x,\kappa_y)$:

$$S(\kappa_x,\kappa_y,\omega) = S(\kappa_x,\kappa_y)\delta(\omega - \omega_+) , \tag{12:10}$$

where ω_+ is given in (12:7) and $\delta(u)$ is the Dirac impulse function of argument u. The normalization here is such that the mean-square surface height is

$$h^2 \equiv \langle \zeta^2 \rangle = \int_{-\infty}^{\infty} d\kappa_x \int_{-\infty}^{\infty} d\kappa_y \int_{-\infty}^{\infty} d\omega\, S(\kappa_x,\kappa_y,\omega) = \int_{-\infty}^{\infty} d\kappa_x \int_{-\infty}^{\infty} d\kappa_y\, S(\kappa_x,\kappa_y) . \tag{12:11}$$

One can define a non-directional temporal spectrum $S(\omega)$ as follows:

$$S(\omega) = \int_{-\infty}^{\infty} d\kappa_x \int_{-\infty}^{\infty} d\kappa_y\; S(\kappa_y,\kappa_y,\omega) = \int_{-\infty}^{\infty} d\kappa_x \int_{-\infty}^{\infty} d\kappa_y\; S(\kappa_x,\kappa_y)\delta(\omega - \omega_+) \tag{12:12}$$

It turns out that oceanographers can conveniently measure $S(\omega)$ directly in a number of ways. For a review of these techniques, see Kinsman (1965). Many have reported detailed observations of $S(\omega)$ for wind-driven ocean waves. Others have attempted to fit empirical laws to these observations to relate the spectrum to the wind speed. One such set of observations is shown in (F12.3a) taken from Moskowitz (1964); these carefully selected spectra for deep-water waves are fully developed only at wind speeds below 30 knots, however. Moskowitz notes that on the open seas, the fetch and duration are rarely sufficient for winds above 30 knots that the sea will reach a fully developed condition. Thus observed spectra at these higher winds will usually be lower than models developed for fully developed seas.

Several semi-empirical models for wind-wave spectra enjoy popularity; among them are the Neumann-Pierson, the Pierson-Moskowitz, and the Phillips spectra (Kinsman, 1965). These differ chiefly in the form postulated for the lower-end cutoff. Because of its mathematical simplicity and for general lack of detailed information about the cutoff (which is observed to be quite steep in the absence of swell), we shall here employ the Phillips model when this function is needed for quantitative estimates. Furthermore, since observations indicate that a specific directionality is difficult to justify (Phillips, 1966; Munk and Nierenberg, 1969), we shall assume that the model is semi-isotropic. This means that all directions in the +x half-space are equally favored in amplitude by the waves. This model then has the form

$$S(\kappa_x,\kappa_y) = \begin{cases} B/\left[2\pi\left(\kappa_x^2 + \kappa_y^2\right)^2\right] \text{ for } \kappa \equiv \sqrt{\kappa_x^2 + \kappa_x^2} > g/u^2 \\ \\ 0 \text{ for } \kappa \equiv \sqrt{\kappa_x^2 + \kappa_y^2} < g/u^2 \end{cases} \tag{12:13}$$

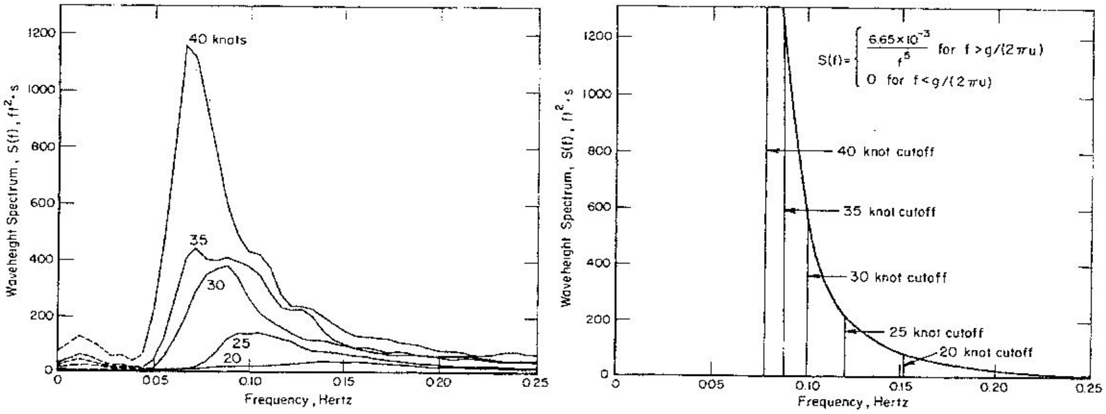

Figure 12.3 *Measured and model waveheight temporal spectra. (a) Measured [after Moskowitz, 1964]; seas are not fully developed at winds above 25 knots. (b) Phillips model for fully developed seas.*

where B is a dimensionless constant observed by Phillips (1966) and others to be approximately 0.005. Energy in this spectrum is spread symmetrically over both positive and negative wavenumbers. The above model shows the spectral saturation observed when the wavenumber κ exceeds the lower-end cutoff, given in terms of the wind speed u by g/u^2. In this saturated region—often called the equilibrium region—the Phillips spectrum follows a κ^{-4} law.

From (12:13) and (12:12), the temporal non-directional version of the Phillips model is found to be:

$$S(\omega) = \begin{cases} g^2 B/\omega^5 \text{ for } \omega > g/u \\ \\ 0 \text{ for } \omega < g/u\,, \end{cases} \tag{12:14}$$

where again the energy is distributed symmetrically for $\pm\omega$. Figure (12.3b) shows plots of (12:14) for comparison with spectra observed by Moskowitz.

Physically, our Phillips model implies that the wind does not affect the shape of the spectrum in the equilibrium region. As the wind increases it merely drives the cutoff lower, piling up more energy beneath the spectrum (and increasing the rms waveheight). This assumes of course that one waits until the seas are fully developed at a given wind speed. The reason for this effect on the lower-end cutoff can be explained simply. The longest (and hence fastest) waves which can be excited by the wind are those whose phase velocity, v, matches the wind speed u. The length of these waves is given by the dispersion relationship (12:3): $[(gL_{CO})/(2\pi)] = (g/\kappa_{CO}) = v^2 = u^2$. Solving this for κ_{CO}, we obtain g/u^2, the sinusoid with the smallest (or cutoff) wavenumber which is excited by the wind with speed u.

12.1.5 RMS Height and Slope of Wind Waves

The rms (or significant) waveheight, as mentioned previously, is the essence of sea state. The rms slope of water waves, while not as directly indicative of sea state, appears frequently in scatter theories, especially specular point theories for microwave frequencies. Hence it is desirable to have quantitative estimates of the dependence of each on wind speed for fully developed seas.

The mean-square waveheight, h^2, can be obtained directly from (12:11) by using the Phillips spectrum (12:13). This gives

$$h^2 = \frac{Bu^4}{2g^2}\,m^2 \ , \text{ or } h = .016u^2 m \ , \tag{12:15}$$

where $B = 0.005$ (a dimensionless constant), u = windspeed (m/s), and g is the acceleration gravity (9.81 m/s^2).

The mean-square slope can be obtained in a similar manner. Since we have already assumed a *semi-isotropic* directional pattern for the Phillips spectrum, we have $<\zeta_x^2> = <\zeta_y^2> = \frac{1}{2}<\zeta_x^2 + \zeta_y^2> = \frac{1}{2}s^2$, where s^2 is the *total* slope at a point on the surface. We obtain a result for s^2—after integration of the Phillips spectrum—which depends upon the upper (as well as the lower) bound on the spectrum. If one is interested only in the slope of the gravity waves, then it makes sense to take as the upper limit $\kappa_c \simeq 0.038\ m^{-1}$, the boundary between the gravity and capillary wave regions. We then have

$$s^2 = B\ \ell n\left(\frac{\kappa_c u^2}{g}\right), \tag{12:16}$$

Often in the specular point theories applicable at microwave and higher frequencies, the slopes of the capillary waves do in fact affect the magnitude of the scatter. In this case, the mean-square slope should include these capillaries. Phillips (1966) and Miles (1962) show that for high winds, about half of the mean-square slope comes from the capillaries, and one needs to add a term to (12:16) for $u > 5$ m/s to account for viscous dissipation. This correction term is

$$s_c{}^2 = B'\ \ell n\left(\frac{\kappa_\nu}{\kappa_c}\right), \tag{12:17}$$

where $B' = 0.015$ (dimensionless), $\kappa_\nu \simeq 3.2\ u^{8/5}\ cm^{-1}$, and as before $\kappa_c \simeq 3.8\ cm^{-1}$.

A simpler empirical relationship derived from (F4.17) of Phillips (1966) can be obtained which includes the effect of capillary slopes as well as the slopes of the gravity waves. It is valid roughly for $1\ m/s < u < 15\ m/s$.

$$s^2 \simeq 5.5 \times 10^{-3} u \ , \text{ or } s = 0.074\sqrt{u}\ . \tag{12:18}$$

12.2 MF/HF Radar Scatter from the Sea

One of the more thoroughly established radar techniques for remote sensing of sea wave characteristics uses frequencies in the MF and HF regions. Recent quantitative theories, confirmed by a variety of experimental configurations, lend considerable credence to the concept. We review first the physical mechanism and theoretically predicted echo strength, and then apply these results to several monostatic and bistatic concepts at MF and HF. Supporting experimental data for these techniques is presented where available.

12.2.1 Predicted Magnitude and Physical Nature of Sea Echo at MF/HF

Sea echo at frequencies below VHF has been observed by radars since World War II. Crombie (1955) appears to have been the first to correctly deduce the physical mechanism responsible for this sea scatter. Based upon HF experimental observations of the backscatter Doppler signal spectrum, he noted that—in contrast with a typical noiselike clutter—the sea echo always appeared at a discrete frequency shift above and below the HF carrier. These discrete Doppler shifts could not be produced by all of the ocean waves illuminated by the radar, since according to (12:3) waves of different lengths move at different velocities and hence would produce echoes at many Doppler shifts. Thus, working backwards and calculating the ocean wave velocity from the observed discrete Doppler shift, and then the length of the ocean wave traveling at this velocity, he arrived at the following rather startling result: The only ocean wave from the entire spectrum present which produces backscatter at HF has a wavelength precisely one-half the radar wavelength and is moving directly toward and/or away from the radar. The observed Doppler shift of the sea return was seen to increase with the square root of the carrier-frequency—rather than in direct proportion, as with a discrete moving target—further confirming this explanation (following the square-root relationship between velocity and length of gravity waves, as given in (12.3)). Hence the experimentally deduced mechanism was seen to be "Bragg scatter", the same phenomenon responsible for scatter of X-rays in crystals and light rays from diffraction gratings and holograms.

Quantitative theoretical analyses of the scatter problem lagged these experimental deductions by several years. Peake (1959) appears to have been the first to reduce the classic statistical boundary perturbation theory of Rice (1951) to σ°, the normalized average scattering cross section per unit area for a slightly rough surface. Barrick and Peake (1968) noted that this result, when interpreted, shows that scatter is produced by the Bragg mechanism, in agreement with Crombie's deductions. Based upon a deterministic analysis of backscatter from sinusoidal waves, Wait (1966) independently obtained a result which was explainable via Bragg scatter.

No attempt was made until very recently to apply these scatter theories to the sea, which, as we have seen in the preceding section, has a unique waveheight spectrum and simple first-order dispersion relationship between spatial and temporal ocean wavenumbers. Barrick (1970, 1972) and Crombie (1971) both have obtained quantitative predictions for the scattered signal spectrum for sea echo, including the temporal variation and the dispersion relationship for the ocean waveheight. The results and notation of Barrick are somewhat more general and will be employed in this chapter; Crombie's solution for backscatter agrees both quantitatively and qualitatively with Barrick's, serving as an independent check.

The technique used by Barrick was initially applied by Rayleigh to scatter of acoustic waves from a sinusoidal surface. It was generalized by Rice to permit the analysis of the average electromagnetic signal intensity scattered from a randomly rough surface. Basically, one employs a Fourier series expansion for the surface, as given in (12:6), and then expands the three components of the electromagnetic field above the surface into the same type of series with the same wavenumbers (am, an wk), but with unknown coefficients. These coefficients are then determined by enforcing the boundary conditions at the surface. The fields at the boundary are expanded in a perturbational manner, permitting an ordering of the terms and a straight-forward solution for the unknown field coefficients. Mathematical details are found in Rice (1951), Peake (1959), and Barrick (1970, 1972).

This boundary perturbation approach requires the assumption of the following limitations in order to be *mathematically* valid: (i) the height of the surface must be small in terms of the radio wavelength, (ii) surface slopes must be small compared to unity, and (iii) the impedance of the surface medium must be small in terms of the free space wave impedance. These conditions are all satisfied by the sea below mid-VHF.

The solutions obtained from the Rice perturbation technique possess some similarity to those obtained earlier by Davies (1954) for a slightly rough surface using a physical optics technique. The perturbation results are superior, however, for two reasons: (i) they contain polarization dependence and correctly predict near-grazing scatter for vertical polarization, whereas physical optics does not, and (ii) they are mathematically valid in the low-frequency limit (as wavelength approaches infinity), whereas the physical optics approximation will eventually fail its inherent requirement that surface radii of curvature be much larger than wavelength.

Before giving the solutions for the scattering coefficients of the sea, we first review the radar range equations for average received power and its spectral density scattered from a patch of sea of area dS:

$$\left.\begin{array}{r} dP_R(\omega) \\ \\ dP_R \end{array}\right\} = \frac{P_T G_T G_R \lambda^2}{(4\pi)^3 R_R^2 R_T^2} F_T^2 F_R^2 \, dS \times \left\{\begin{array}{ll} \sigma(\omega) & \text{W/rad/s} \\ \\ \sigma^0 & \text{W}, \end{array}\right. \qquad (12:19)$$

where P_T is the transmitted power, R_R and R_T are the ranges from the scattering patch dS to the receiver and transmitter respectively, and λ is the radar wavelength. The quantities F_T and F_R are the Norton attenuation factors between the patch and the transmitter and receiver for TM propagation near the surface; they account for any propagation losses greater than the normal free-space ($1/R^2$) spreading losses, and hence approach unity for a perfectly conducting flat earth. One must be cautious in defining the antenna gains G_T and G_R in the direction of the scattering patch. For ground-wave or line-of-sight propagation to and from the patch, G_T and G_R must be the *equivalent* free-space gains of the antenna; that gain is less than its measured gain in the presence of the conducting ground by 6 dB. For example, a vertical quarter-wave monopole fed against the ground would have an equivalent free-space gain for use in (12:19) of −0.85 dB rather than +5.15 dB. For over-the-horizon ionospheric propagation to the patch, however, one employs the normal gains of the antenna measured in the presence of the ground (e.g., +5.15 dB for the quarter-wave monopole)†.

The actual average scattering cross section for the patch of sea within the radar resolution cell of area $dS(m^2)$ is then $\sigma^0 dS(m^2)$. Hence, σ^0 is the average scattering cross section of the sea per unit area. Its counterpart in the equation for received power spectral density is $\sigma(\omega)$, the average scattering cross section per unit area per rad/s bandwidth. The normalization used here is such that $\sigma^0 = \frac{1}{2}\int_{-\infty}^{\infty} \sigma(\omega)d\omega$.

Referring to (F12.4) which defines the incidence and scattering angles at the sea surface patch dS, we can write the following expressions for $\sigma(\omega)$ and σ^0 *for vertically incident and vertically scattered polarization* (Barrick, 1972):

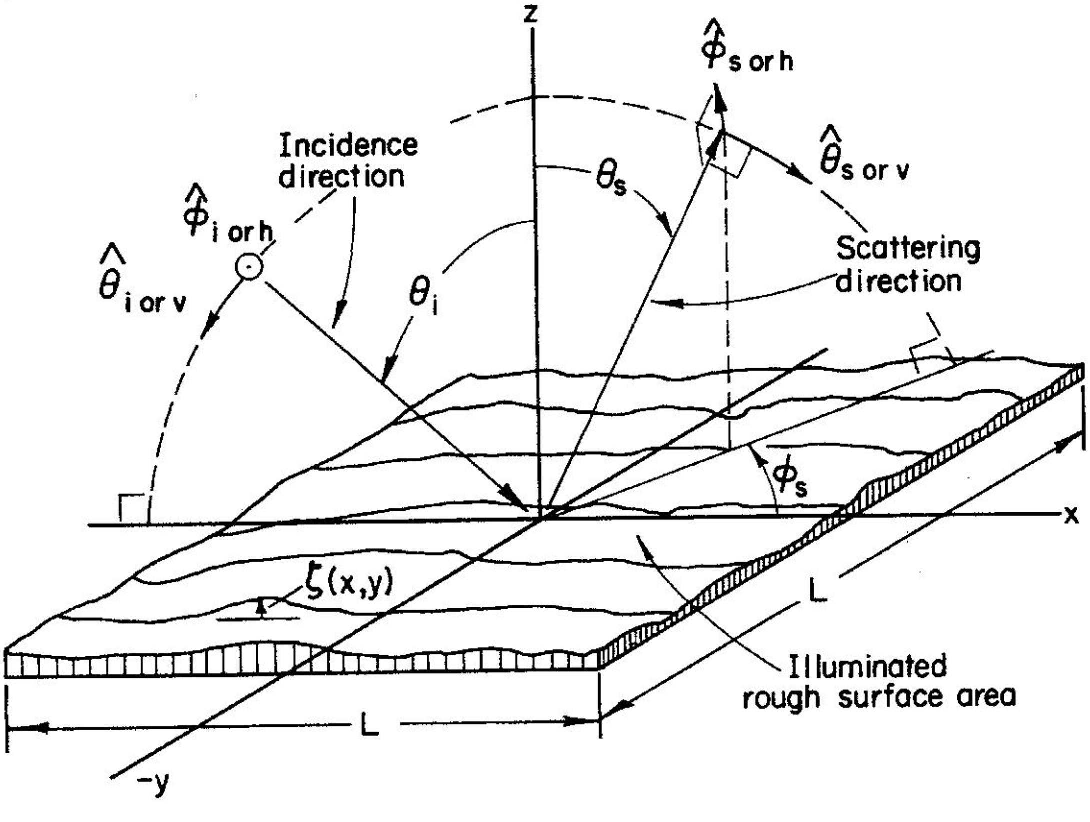

Figure 12.4 *Local geometry near scattering patch.*

---

† Any ionospheric attenuation losses could in this case be absorbed in a factor similar to $F_T^2 F_R^2$.

$$\left.\begin{array}{r}\sigma_{vv}(\omega)\\ \\ \sigma^0_{vv}\end{array}\right\} = 4\pi k_0^4(\sin\theta_i\sin\theta_s - \cos\varphi_s)^2 \times \begin{cases} W[k_0(\sin\theta_s\cos\varphi_s - \sin\theta_i),\, k_0\sin\theta_s\sin\varphi_s,\, \omega - \omega_0] \\ W[k_0(\sin\theta_s\cos\varphi_s - \sin\theta_i),\, k_0\sin\theta_s\sin\varphi_s]\ , \end{cases} \tag{12:20}$$

where $k_0 = 2\pi/\lambda$ is the radio wavenumber, ω_0 is the radiant carrier frequency, and $W(\kappa_x,\kappa_y,\omega)$, $W(\kappa_x,\kappa_y)$ are the first-order spatial/temporal and spatial waveheight spectra of the sea, respectively; they are related to the spectra defined in (12.1.4) by[†]

$$W(\kappa_x,\kappa_y,\omega) = 2^3 S(\kappa_x,\kappa_y,\omega);\ W(\kappa_x,\kappa_y) = 2^2 S(\kappa_x,\kappa_y)\ . \tag{12:21}$$

Equation (12:20) was derived assuming that the scattering patch is perfectly conducting. For the sea at MF/HF, this approximation is quite valid. The only seemingly confusing issue is the fact that when either the incident or scatter polarization state is vertical, and when the propagation angle for that polarization state approaches grazing, the scattered power remains finite. For a finitely conducting surface medium, the result analogous to (12:20) would always approach zero at grazing. This apparent difference is reconciled by Barrick (1972); the effect of finite conductivity *for vertical polarization* is separated from the scattering cross section and expressed as the Norton attenuation factors, F_T and F_R, in (12:19). Since vertical polarization is the only mode which can propagate efficiently as a ground-wave near the sea at MF/HF, most experiments would logically employ vertical (or TM) if one or the other paths to the scatter patch grazes the sea surface. Hence, one can handle the analysis of such an experiment by treating the sea surface patch as perfectly conducting, and then accounting for the finite conductivity by employing the Norton factors F_T and/or F_R, depending upon whether the incident and/or scatter states are vertically polarized.

If one or the other or both polarization states are not vertical, one can modify (12:20) in the following manner to give the other three cross sections and spectra for the sea[††]: $\sigma_{vh}(\omega)/\sigma^0_{vh}$, $\sigma_{hv}(\omega)/\sigma^0_{hv}$, and $\sigma_{hh}(\omega)/\sigma^0_{hh}$ are obtained by replacing the factor $(\sin\theta_i\sin\theta_s - \cos\varphi_s)^2$ in (12:20) by $(\cos\theta_i\sin\varphi_s)^2$, $(\cos\theta_s\sin\varphi_s)^2$, and $(\cos\theta_i\cos\theta_s\sin\varphi_s)^2$, respectively. Thus the dependence of scatter upon the nature of the roughness is the same for any polarization state; it is contained in the surface height spatial/temporal spectrum.

Physically (12:20) is interpreted as follows. The ocean spatial wavenumbers (κ_x,κ_y) which are producing scatter are given in terms of the radio wavenumber, k_0, and observation angles θ_i, θ_s, φ_s by $\kappa_x = k_0(\sin\theta_s\cos\varphi_s - \sin\theta_i)$ and $\kappa_y = k_0\sin\theta_s\sin\varphi_s$. These, however, are precisely the wavenumbers required of a diffraction grating which is to scatter a wave incident from θ_i into a direction θ_s, φ_s. Hence, the theory shows that the ocean surface produces scatter by the simple Bragg mechanism, which confirms the experimental deductions of Crombie (1955). Furthermore (12:20) implies that, in order to measure the directional spectrum of the sea, one can measure the sea echo (i.e., $\sigma(\omega)$ or σ^0) and vary k_0, θ_i, θ_s, or φ_s in whatever manner is most convenient experimentally. Different schemes which vary one or more of these quantities are to be examined in the following subsections.

Having the radar range equation (12:19) and the expression for the sea scatter cross sections (12:20), one can now analyze any monostatic or bistatic configuration by integrating (12:19) over the area illuminated within the radar range cell and/or beam. Examples will be considered later. To obtain estimates for the received sea-scatter power magnitude for quantitative system design, one can employ the Phillips spectrum (12:13) in (12:20). Use of this spectrum for sufficiently high wind speeds (such that $u^2 > gk_0 \times \sqrt{\sin^2\theta_i - 2\sin\theta_i\sin\theta_s\cos\varphi_s + \sin^2\theta_s}$) provides an upper limit on received power; for winds and seas which are lower, the received power will be always less than this amount.

[†] We apologize for the inconsistency in notation for the waveheight spectrum. Unfortunately, oceanographers independently established the convention using S, while scattering analysts adopted the Rice convention based upon W. Both are currently found in the literature, depending upon the discipline preferred by the user. Consequently, we employ both here and give the connection between them to facilitate reference to other works.

[††] The first subscript always refers to the polarization state of the incident wave, while the second denotes the state for the scattered wave of interest.

12.2.2 Backscatter MF/HF Experiments

We consider in this section possible backscatter experiments employing MF/HF radars. These are in almost all cases either surface-based ground-wave or ionospheric sky-wave configurations. In both situations, $\varphi_s \to \pi$ and θ_i, θ_s are sufficiently close to grazing (i.e., within 20°) that the sin θ factors appearing in (12:20) can be replaced by unity. We then have

$$\left.\begin{matrix}\sigma_{VV}(\omega) \\ \\ \sigma^0_{VV}\end{matrix}\right\} = 16\pi k_0^4 \times \left\{\begin{matrix}W(-2k_0, 0, \omega - \omega_0) \\ \\ W(-2k_0, 0) .\end{matrix}\right. \tag{12:22}$$

It is understood of course that the waveheight spectrum wavenumbers κ_x and κ_y (in the x,y directions) are defined *at the scattering patch dS*. Hence, as one integrates (12:19) over the surface S, (12:22) implies that the x-y axis at the patch remain constant with respect to the radar line of sight, and therefore must rotate as the line of sight changes in azimuthal position on the ocean. Thus, as one swings the radar beam by 90°, he is not only looking at a different patch of ocean, but with the κ_x, κ_y wavenumber positions in (12:22) interchanged.

Let us first calculate $\sigma_{VV}(\omega)$ and σ^0_{VV} based upon the fully developed Phillips spectrum model, and compare these predictions with experimental evidence. Using (12:13) in (12:22), we have

$$\sigma_{VV}(\omega) = 4 \times 10^{-2} \delta(\omega - \omega_0 + \sqrt{2gk_0}) ,$$

$$\sigma^0_{VV} = 0.02 = -17 \text{dB} . \tag{12:23}$$

It was initially assumed that waves were traveling only in the +x direction (away from the radar). If waves are also moving into the $-x$ half-space (toward the radar), then we have an impulse function at $\omega = \omega_0 + \sqrt{2gk_0}$, as well as the one at $\omega = \omega_0 - \sqrt{2gk_0}$ shown above. Thus one sees that in general, according to the first-order theory, all of the energy backscattered is contained at two discrete Doppler shifts $(\pm\sqrt{2gk_0})$ from the carrier. Secondly, the magnitude of σ^0_{VV}, the average backscattered cross section per unit area, has as its upper limit −17 dB, as defined according to (12:19).

Let us now compare both of these predictions with experimental evidence based upon ground-wave radar configurations. One set of recent ground-wave measurements of sea backscatter was made by Headrick of the Naval Research Laboratory (Barrick, 1972) at 10.087 MHz, in which he obtained measurements of σ^0_{VV}. In the experiment, two vertical monopoles were located near Annapolis, Maryland, on the upper Chesapeake Bay. Spectral processing permitted separation of water-wave scatter from stationary ground clutter echoes. The signal format used provided a 20 nmi range resolution cell. The Norton attenuation factor F_R ($=F_T$) was calculated for four range cells at different distances on the bay using the pertinent water conductivity (i.e., ~ 2 mho/m).

Data were recorded and processed on February 4, 1969, a day on which a moderate wind was blowing from the north. Waves receding from the radar were observed to be stronger due to the wind, and water waves of the Bragg scatter length $\lambda/2$ (15 m in this case) were estimated to be fully developed. The average received power from the water was processed at four ranges down the bay: 45, 55, 67, and 75 nmi. Propagation to all of these points was via groundwave since they were all below the radio horizon; thus one must compare measurements with σ^0_{VV} at grazing incidence, as given in (12:22) or (12:23). With the water area within each resolution cell (i.e., dS) estimated from maps of the bay, this factor—as well as the Norton attenuation factors—were removed from the radar equation. This yielded experimental values for σ^0_{VV} of −17 dB at all four ranges†.

The fact that the 15 m long water waves were fully developed (only a 9.4 knot wind is required to arouse waves of this length) means that the backscatter might have been expected to approach the Phillips saturation estimate in (12:23) as an upper limit. The agreement between measured and predicted values of σ^0_{VV} not only lends credence to the theory, but confirms the oceanographic estimate of the "Phillips saturation constant", $B = 0.5 \times 10^{-2}$ used in (12:13).

---

† Headrick employs the actual antenna gains rather than their effective free space gains. Hence his reported values of −29 dB with (12:19) correspond to σ^0_{VV} of −17 dB by our definition −6dB caused by each antenna.

As further evidence of the validity of the first-order theory for ocean-wave scatter, we cite recent HF measurements by Crombie et al. (1970) from Barbados Island in the West Indies. Again the antennas were located near the water so that propagation to ranges beyond the horizon was via ground wave. In this case we examine Crombie's received signal spectrum; a very high spectral resolution of 0.002 Hz was obtained with digital signal processing. Backscatter was received with broad-band vertical monopole antennas from the half-space toward the east.

Shown in (F12.5) are the relative received power spectra measured simultaneously on August 15, 1969, at 2.9 and 8.37 MHz from the range cell at 45 km. Coherent processing at a 0.5 Hz offset (removed in the figures here) permits both negative and positive shifts above the carrier to be observed. The first-order peaks (corresponding to our impulse functions in (12:23)) occur as predicted at ±0.174 Hz from the 2.9 MHz carrier and ±0.296 Hz at 8.37 MHz. The relative strength of the positive spike over the negative spike at both frequencies agrees with the dominant wind direction in this area; trade winds from the east should excite west-moving water waves, producing a positive Doppler shift. Lesser spikes in the records at 0.0 Hz, +0.25 Hz for 2.9 MHz and at +0.42 Hz for 8.37 MHz are attributed by Crombie as due to higher-order hydrodynamic and electromagnetic contributions. Theory of such processes is examined in a later subsection.

We turn attention now to two ground-wave backscatter experiments which can be used to measure the waveheight spectrum of the ocean. In both cases, one must vary the frequency (and hence the Bragg wavenumber, $2k_o$) which samples the ocean waveheight spectrum in (12:22) over its significant lower end. If we assume that the spectrum cuts off at a wavenumber *somewhere* near g/u^2 ($g = 9.81$ m/s^2, u = wind speed, m/s,) then for higher winds and seas one must use lower frequencies. A plot of the backscatter radar frequency required versus wind speed is given in (F12.6); one of course should actually employ a frequency lower than this (by possibly 20 percent) to ascertain the spectral behavior below cutoff.

The first experiment, discussed and tested by Crombie (1971), employs azimuthally omnidirectional antennas on the coast. Using pulsed signals and a range gate set at 22.5 km from the radar, Crombie obtained the average received power at as many as eight frequencies, ranging between 1.7 MHz and 12.3 MHz. With such an experiment, one is simultaneously observing sea scatter from a semi-circular annulus, and it is assumed that the sea is relatively homogeneous over such a circle (i.e., that the directional ocean waveheight spectrum is essentially constant over 45 km). This assumption is reasonable for on-shore winds and waves; for off-shore winds, however, the limited fetch does not permit the waves nearer the shore to build up as high as those more distant. Crombie (1971) notes that even at 100 km, higher off-shore waves may still not be fully developed. Hence if one spectrally processes the signals and employs the energy only in the Doppler line *above* the carrier, the homogeneity assumption should be valid.

Since the antennas in this experiment are azimuthally omni-directional and since the received energy from everywhere in the semi-circular annulus occurs at the same ± Doppler shift, it is not possible to obtain the *directional* waveheight spectrum. One can obtain the non-directional waveheight temporal spectrum, which was defined in (12:12) and exemplified in (F12.3). To do this and relate $S(\omega)$ to the received power, P_R, at carrier frequency f_o, one must integrate the second version of (12:19) over the semi-circular annulus, using (12:22) and (12:12). The one-sided spectral result is

$$S\left(\sqrt{4\pi g f_o/c}\right) = \frac{4R^3}{\Delta R}\,\frac{P_R}{P_T}\left(G_T G_R F^4 \sqrt{4\pi g f_o/c}\right)^{-1} \text{m}^2/\text{rad/s} \qquad (12:24)$$

where c is the free-space radio wave velocity and ΔR is the width of the range-resolution cell. It must be noted that several of the factors on the right side of (12:23) may vary with frequency, including antenna gains, transmitted power, and the Norton attenuation factors.

Shown in (F12.7) are several such temporal spectra reduced by Crombie from observations off Barbados Island in the West Indies (plotted versus Hertz rather than rad/s). In the upper two, he was able to compare the predicted significant waveheight (obtained from integrating the area under the spectrum) with laser profilometer measurements of significant waveheights; the agreement is good. In the bottom plot, Crombie shows also a Pierson-Moskowitz model spectrum predicted for a 20 knot wind and fully developed seas for comparison. Crombie cautions that the spectra to the left of the line marked "minimum observed frequency" are estimated; in the upper pair of records, the estimated portion is a substantial portion of the area under the curves. This points up the importance of employing a sufficiently low (MF) frequency if one wishes to obtain spectral detail in higher sea states.

A variation of the above backscatter experiment can provide the directional rather than merely the non-directional waveheight spectrum. The azimuthally omni-directional antenna is placed on a moving ship at

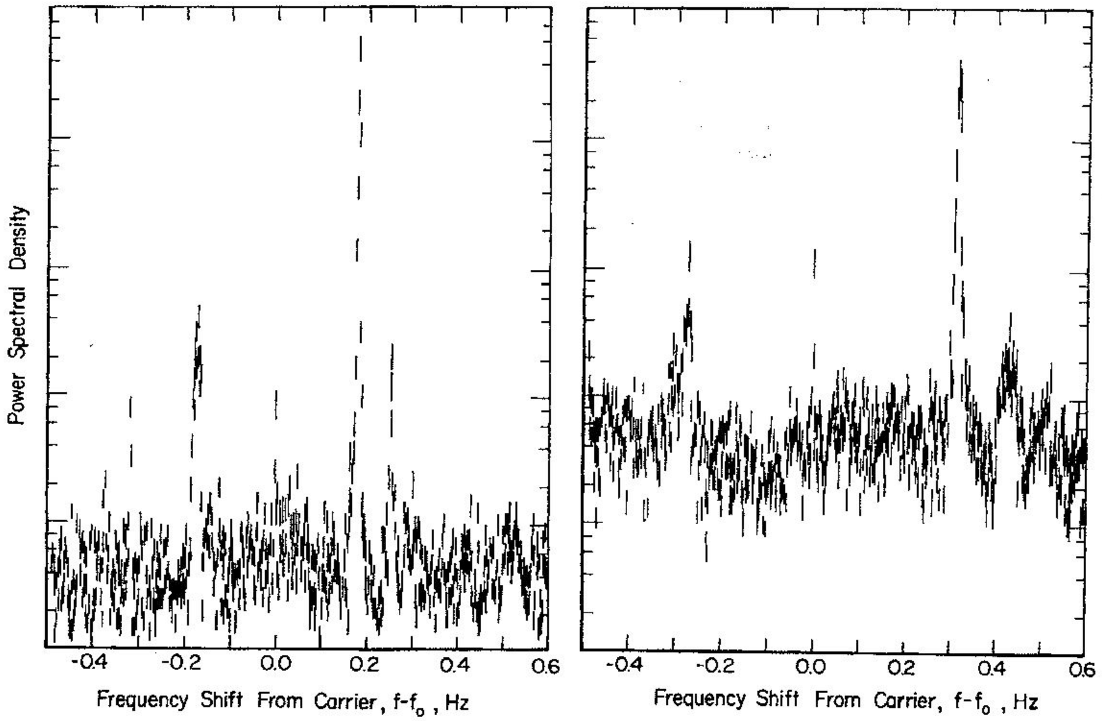

Figure 12.5 *Measured backscatter signal Doppler spectra of HF sea echo (after Crombie et al., 1970) (a) 2.9 MHz carrier frequency (b) 8.37 MHz carrier frequency.*

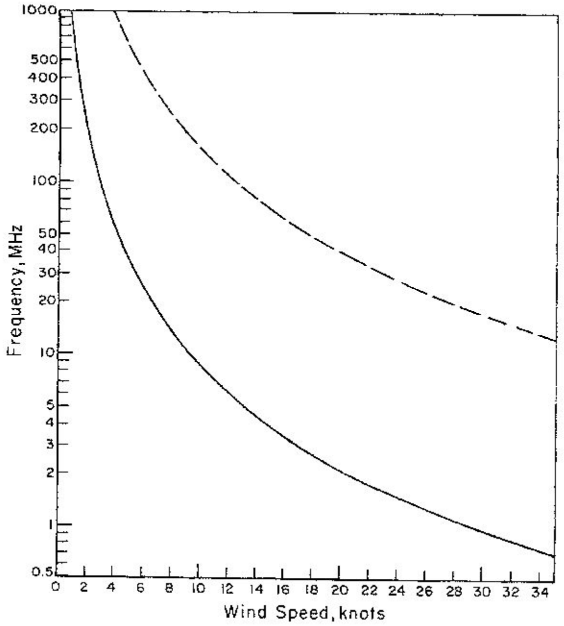

Figure 12.6 *Solid curve gives frequency necessary to observe lower end (cutoff) of gravity wave spectrum for near-grazing backscatter; dashed curve gives frequency limit where slightly rough surface model fails mathematically for given wind speed.*

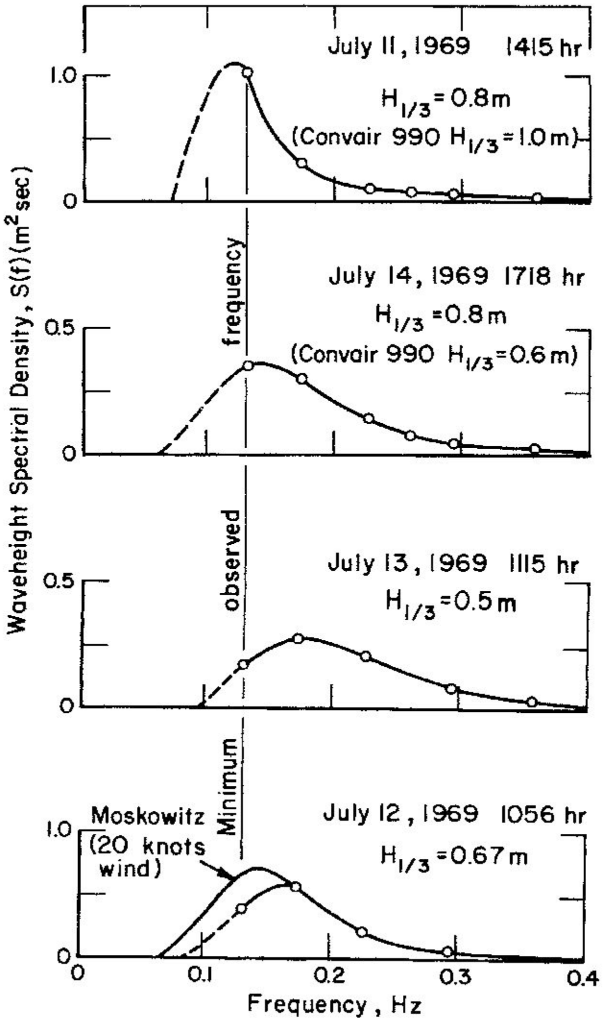

Figure 12.7 *Temporal waveheight spectra deduced from MF/HF ground-wave backscatter observations (after Crombie, 1971).*

sea. In this case the sea return does not appear at the previous single set of unique Bragg Doppler shifts around the carrier, for the ship's motion introduces a different Doppler bias on the return from each point around the range ring. This Doppler shift is $\omega_{sh} = 2\omega_o v_{sh} \cos\theta/c$, where v_{sh} is the ship speed and θ is the angle from the ship's bow to a point on the range ring. We assume again that the ocean waves are moving predominantly into one half-space and that the "sea state" is homogeneous over the area of the ring. Then the one-sided power spectral density from a given element of area on the ring (i.e., dS = RΔRΔθ) is found from (12:19) and (12:22) to be

$$dP_R(\omega) = \frac{2^4 P_T G_T G_R F^4 \Delta R \Delta\theta}{k_o^2 R^3} S(2k_o \cos\theta, 2k_o \sin\theta)\delta(\omega - \omega_o \pm \omega_+ - \omega_m \cos\theta)\,, \quad (12:25)$$

where $\omega_m = 2\omega_o v_{sh}/c$ is the maximum ship-induced Doppler shift and $\omega_+ = \sqrt{2gk_o}$ is the Doppler shift from the gravity waves. To obtain the average power density spectrum, $P_R(\omega)$, from (12:25) we must integrate over θ. The resulting one-sided spectrum $P_R(\omega)$ is seen to consist of two "pedestals", each centered at $\omega_o \mp \sqrt{2gk_o}$. Thus one can relate the spatial directional waveheight spectrum, $S(\kappa_x,\kappa_y)$ to, say, $P_R(\omega)$ within the positive pedestal at $\omega_o + \quad 2gk_o$ as follows:

$$S\left(2k_o\eta/\omega_m, 2k_o\sqrt{1 - \eta^2/\omega_m{}^2}\right) = \frac{R^3 k_o{}^2}{2^4 \Delta R G_T G_R F^4} \sqrt{\omega_m{}^2 - \eta^2} \frac{P_R(\omega)}{P_T}, \tag{12:26}$$

where $\eta = \omega - \omega_o - \sqrt{2gk_o}$, and where it is understood that $P_R(\omega)$ is non-zero only within the pedestal region, i.e., $|\eta| \leqslant \omega_m$.

Thus, by examining the received power density spectrum $P_R(\omega)$, one can obtain the directional spatial spectrum of ocean waves for spatial wavenumbers $\kappa_x = 2k_o \cos\theta$, $\kappa_y = 2k_o \sin\theta$ over all θ by noting that $\cos\theta = \eta/\omega_m$ and $\sin\theta = \sqrt{1 = \eta^2/\omega_m^2}$. As in the preceding experiment, one must vary the carrier frequency (or k_o) to sample the spectrum at a different *total* wavenumber, κ ($\kappa = \sqrt{\kappa_x^2 + \kappa_y^2} = 2k_o$). Also, it must be noted that there is an ambiguity with this technique, for waves propagating symmetrically with respect to the ship axis (i.e., $\pm\theta$) will be indistinguishable in their Doppler characteristics. Ship course changes can readily resolve this ambiguity, however.

Up to now, we have discussed only ground-wave backscatter radar sensors. These are limited in range to perhaps 100-200 km around the radar. Several investigators have recognized the potential of sky-wave (ionospheric) radars as remote ocean wave sensors (Tveten, 1967), (Ward, 1969), (Hasselmann, 1971); such shore-based radars could look at ocean areas as remote as 3200 km away. Since the normal range of elevation (or grazing) angles with ionospheric radars is usually 20° or less, (12:22) is adequate to describe ionospheric backscatter from the ocean.

As an example of ionospherically-propagated sea backscatter, we show in (F12.8) an averaged spectrum made by Barnum (1971) using a wide-aperture antenna at SRI in California, looking into the Pacific Ocean. Averaging was done over 16 range cells, each of which was approximately 1 km long by 10 km wide. At the particular time this record was made (~1500 local time, 30 March 1971), the ionosphere was quiet, and the resulting signals are relatively "clean" compared to similar signals under disturbed conditions. The frequency used was 25.75 MHz, the sea area illuminated was ~2700 km from the radar, and the elevation (or grazing) angle was about 6°. Use of coherent integration in the receiver/processor of 25.6 s permitted a spectral resolution of approximately 0.04 Hz.

The predicted first-order Bragg backscattered Doppler shifts at 25.75 MHz should occur at ±0.518 Hz from the carrier. It should be noted from (F12.8) that ionospheric motion imposed an overall shift, or offset, from the carrier of about 0.07 Hz; such offsets are common with ionospheric radars. However, one should note that the distance between the two first-order Bragg lines (2 X 0.158 Hz in this case) is independent of such offsets, and can in fact be used to determine the offset. On the day this sea echo was recorded, Barnum ascertained from weather maps of the illuminated ocean area that the wind (~20 knots) was blowing in a direction 250°, and that seas with 12 ft significant waveheights were reported moving predominantly in a direction 260°. His radar beam was pointed in a direction 242°; hence predominant wave movement was away from the radar, which is confirmed by the preponderance of the negative Doppler components over the positive components. Noted also by Barnum are the positions (relative to that of the first-order Bragg line) of other "higher-order" peaks in the scatter spectrum. Analysis of such higher-order contributions to scatter will be discussed in a subsequent section.

Ionospheric radars hold considerable promise for quick and simple routine monitoring of sea state hundreds of miles from the radar site. Detailed waveheight spectra and directional information on ocean-wave movements are probably not possible with such a radar however. The system sees only those waves in a given part of the ocean moving toward and away from the radar at about one-half the radar wavelength. At a given range and time of day, it is not possible to sweep the frequency of an ionospheric radar over a very wide band due to propagation conditions. During the daytime, one is usually restricted to about 17-30 MHz, while at nighttime one can operate between 9-17 MHz. Hence, the important lower end of the gravity wave spectrum can rarely be observed with an ionospheric radar via first-order Bragg scatter. Recent analyses and interpretations of the higher-order peaks in the received signal spectrum may provide additional useful information on the state of the sea not possible from the first-order Bragg lines. Signal fading and multi-moding in ionospheric propagation at times can produce quite confused spectral records, obscuring

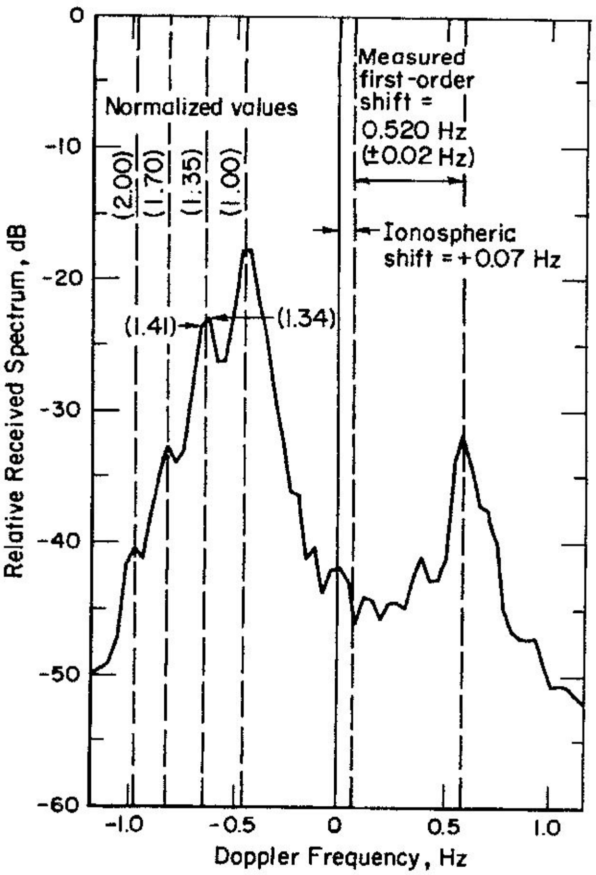

Figure 12.8 *Ionospherically propagated sea backscatter spectrum at 25.75 MHz (after Barnum, 1971).*

higher-order, less prominent peaks. Nonetheless, ionospheric radars—properly exploited—will eventually prove to be valuable remote sensors of sea state.

12.2.3 Bistatic Surface-Based MF/HF Experiments

Upon the discovery of the Bragg effect as the first-order mechanism responsible for sea scatter at MF/HF, several groups independently recognized the potential in bistatic concepts for ocean wave sensing. Unlike backscatter radars, a bistatic radar at a given frequency can measure the strengths of ocean waves of several wavelengths and directions of movement; furthermore, it is possible to relate the scattering ocean wavelengths and directions to the radar observables (namely time delay and Doppler shift). This can be seen by writing the first equation of (12:20) for a bistatic radar with both transmitter and receiver on the surface $(\theta_i = \theta_s = \frac{\pi}{2})$. Using (12:10) in (12:20), we obtain:

$$\sigma_{VV}(\omega) = 2^8 \pi k_0^4 \sin^4\!\left(\frac{\varphi}{2}\right) S[k_0(\cos\varphi - 1),\ k_0 \sin\varphi]\, \delta\!\left[\omega - \omega_0 + \sqrt{2gk \sin(\varphi/2)}\right], \qquad (12{:}27)$$

where 180°$-\varphi$ is the bistatic angle *at the scattering patch* between the lines to the transmitter and receiver. Thus one sees from (12:27) that the sea echo from different patches having different bistatic angles φ will return at different Doppler shifts. Thus it is possible to relate the echo strength at a given Doppler shift to the local sea waveheight directional spectrum evaluated at wavenumbers $\kappa_x = k_0(1 - \cos\varphi)$ and $\kappa_y = k_0 \sin\varphi$.

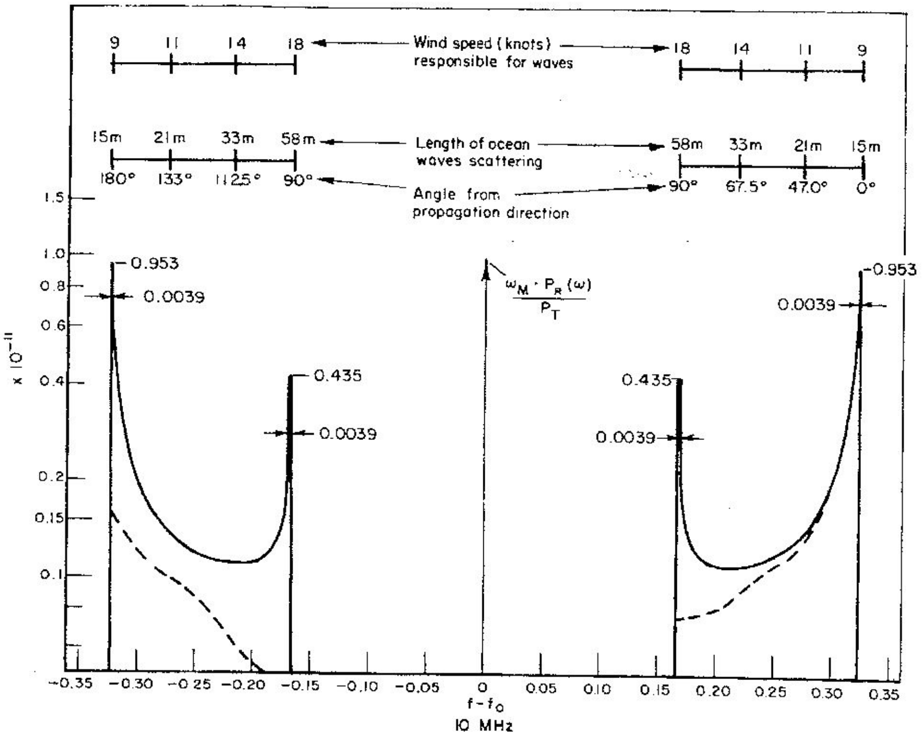

Figure 12.9 *Geometry of bistatic ground-wave MF/HF radar.*

Several investigators have examined such systems: Barrick (1970), Teague (1971) and Nierenberg and Munk (1969) all analyzed the relationships between time-delay and Doppler space (t, f_D) and the Bragg spatial wavenumber space (κ_x, κ_y). Signals arriving at a given time delay in a bistatic radar system are all scattered from an ellipse having the transmitter and receiver points as foci, i.e., $(R_T + R_R)/c = t$, where R_T and R_R are the transmitter-scatterer and scatterer-receiver distances. Such a configuration is shown in (F12.9). To illustrate this transformation, let us normalize the observed Doppler frequency to that for ocean-wave backscatter, i.e., $f_N \equiv f_D/(\sqrt{2gk_0}/2\pi)$. Since the observed Doppler shift, as seen from (12:27) is always greatest for backscatter, we have $0 \leqslant |f_N| \leqslant 1$. Nierenberg and Munk further define a quantity K equal to f_N^2; it is exactly equal to the magnitude of the spatial wavenumber of the ocean waves producing Bragg scatter at a given point divided by $2k_0$. Thus $0 \leqslant K \leqslant 1$, with $K = 1$ occurring for backscatter $(\varphi = \pi)$. The other radar observable, time delay, is also normalized by dividing by t_d, the time delay experienced by the direct signal propagating between the transmitter and receiver separated by distance 2d $(t_d = 2d/c)$: $S \equiv t/t_d$. Then $1 \leqslant S \leqslant \infty$. We also normalize the ocean spatial wavenumbers by dividing them by $2k_0$, i.e., $U = \kappa_x/2k_0$, $V = \kappa_y/2k_0$. Then the transformation relates K or f_N (Doppler shift) and S (time delay) for a point on the elliptical annulus to the ocean wavenumbers U, V responsible for scatter. Since $0 \leqslant |U|, |V| \leqslant 1$, we would like to be able to determine the ocean waveheight spectrum for all U, V in this range by observing K and S. Figures (12.10) and (12.11) show this transformation. The figures show that while it may be possible to find a family of time delays and Doppler shifts corresponding to a given wavenumber, U, it may not be possible to find a single time delay and Doppler shift if one specifies *both* U and V. To be able to do so would mean that the curve for U and the curve for V in terms of S and K intersect somewhere. It can be seen that many of the curves do not in fact cross (e.g., curves of U and V each near unity do not intersect). Furthermore, the confluence of both sets of curves to the upper right indicates that if they *do* cross in this region where they are nearly parallel, accuracy in the practical determination of U, V and S, K will suffer. These equations are explored in greater detail by Teague (1971).

We now proceed to find the general expression for the received signal spectrum $P_R(\omega)$ in terms of the spatial waveheight spectrum of the surface for a given time delay and Doppler shift. This is most easily done

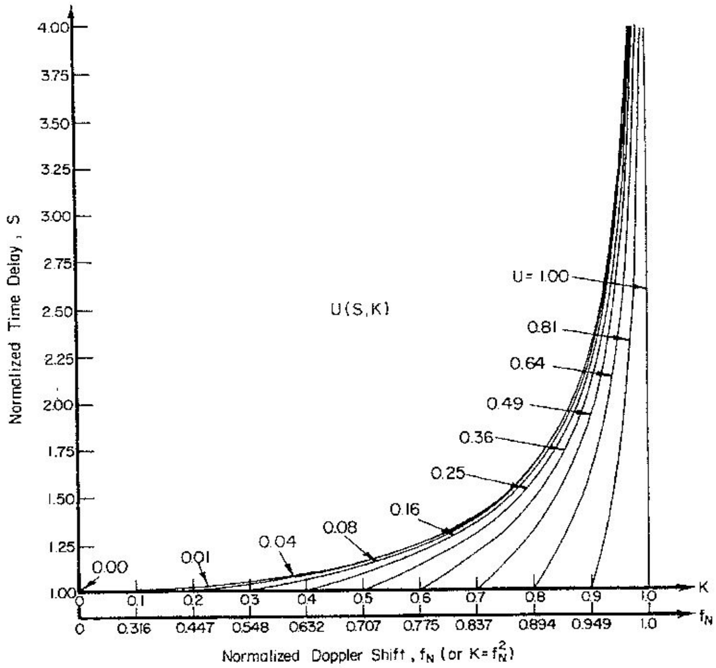

Figure 12.10 *Transformation between U (normalized spatial x-wavenumber), and f_N (normalized Doppler shift) and S (normalized time delay) radar observables.*

by converting to elliptic coordinates, μ, θ and then integrating over θ around a given elliptical annulus. We employ (12:27) in (12:19), but note that the wavenumbers in S of (12:27) are oriented with respect to the incidence direction at a given scattering patch; we must convert these to a space-fixed set of wavenumbers in order to determine a directional waveheight spectrum. The x-direction, and hence κ_x wavenumber direction, for this space-fixed frame is taken as the baseline connecting the receiver and transmitter (i.e., $\theta = 0$). As before, we assume that the sea is homogeneous over the area of an ellipse; this will restrict one in practice to transmitter-receiver separations no greater than about 200 km.

The elliptic coordinate μ can be defined in terms of time delay as $\cosh \mu = t/t_d = S$, where $t_d = 2d/c$ is the transmitter-receiver time of flight. The effective pulse length, τ, defines an elliptical annulus of width $\Delta\mu$ given by $\tau/t_d = \Delta\mu \sinh \mu$. The increment of area—or scattering patch—on the annulus is $dS = R_T R_R \Delta\mu d\theta$; as mentioned above, we intend to integrate over θ. The transmitter and receiver distances at μ, θ, are $R_T = d(\cosh \mu - \cos \theta)$ and $R_R = d(\cosh \mu + \cos \theta)$. We note that in general, transmitter and receiver antennas may be directional, implying that G_T and G_R are functions of μ and θ; we assume here that both antennas are azimuthally isotropic for convenience†. Furthermore, the Norton attenuation factors F_T^2 and F_R^2 are complicated functions of range R_T and R_R. If frequency is restricted to the lower HF and MF region, and transmitter-receiver separation is kept less than 200 km, these factors are approximately unity, a fact which simplifies the integration; we make this assumption also.

We then perform the integration over θ. Two Doppler constants are defined in order to simplify the notation: $\omega_B = \omega_+ \equiv \sqrt{2gk_0}$ and $\omega_S \equiv \sqrt{2gk_0 \tanh \mu}$. The former is the Doppler shift for backscatter, occurring here at the ends of the ellipses. The latter quantity is the Doppler shift which arises from ocean waves at the sides of the ellipse; hence it is the minimum Doppler shift observed for a given time delay. Defining Doppler shift as $\eta = \omega - \omega_0$, we then have a non-zero signal spectrum only for $\omega_S \leqslant |\eta| \leqslant \omega_B$. In terms of these constants and time delay, t (or $\mu = \cosh^{-1}(t/t_d)$, we obtain the following expression for the directional waveheight spectrum as a function of the observed one-sided received power density spectrum:

---

† Field tests of this concept—to be discussed—employed simple isotropic antennas.

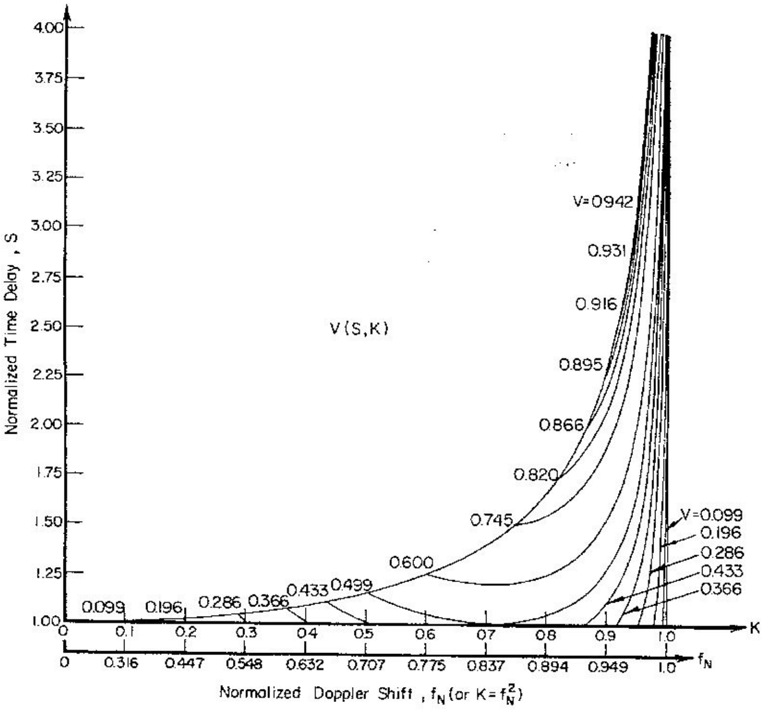

Figure 12.11 *Transformation between V (normalized spatial y-wavenumber), and* f_N *(normalized Doppler shift) and S (normalized time delay) radar observables.*

$$S\left[2k_o \sinh \mu(\eta/\omega_B)^2\sqrt{(\eta/\omega_S)^4 - 1},\ 2k_o \cosh \mu(\eta/\omega_B)^2\sqrt{1 - (\eta/\omega_B)^4}\,\right]$$

$$= \frac{(k_o d)^2}{2^5 G_T G_R}\,\frac{\sinh^2\mu}{\Delta\mu}\,\frac{\sqrt{1 - (\eta/\omega_B)^4}\sqrt{(\eta/\omega_S)^4 - 1}}{(\eta/\omega_B)^{11}}\cdot\frac{\omega_B P_R(\omega)}{P_T}\,. \tag{12:28}$$

In order to obtain a feel for the appearance and magnitude of the received signal spectrum $P_R(\omega)$ with such a system, we employ the Phillips model for the waveheight spectrum of ocean waves, i.e., (12:13). We assume that wind speed is sufficiently great that all ocean waves which can produce scatter are present and fully developed. We employ as antennas two vertical ground-fed quarter-wave monopoles with equivalent free-space gains of 0.82; they are located 2d = 100 km apart. Two frequencies are considered: 5 and 10 MHz. The signal pulse is rectangular in shape and taken as 12.5 μs, and we consider the sea-scattered signal originating from the elliptical annulus at a delay $t = t_d + \tau$, i.e., one pulse length after the arrival of the direct pulse. The signal spectra calculated for this example are shown in (F12.12). Shown there also are the ocean wavelengths, ocean-wave directions with respect to the baseline, and the wind speeds required to excite the waves responsible for scatter at the indicated Doppler shift. The "ears" near the endpoints of the two Doppler pedestals are due to scatter from the "stationary" regions of the ellipse, viz., the sides and ends; they result from the radicals appearing in (12:28). The heights actually observed for these "ears" will depend upon the resolution of the spectral processor, since the area (or energy) contained under them is integrable and finite.

The total sea-scattered power received from this ellipse is approximately $1.5 \times 10^{-11}\ P_T$ at 5 MHz. This should be compared with a received signal power direct from the transmitter of $3.2 \times 10^{-9}\ P_T$. Hence the sea-scattered signal is down about 23 dB from the direct signal at this separation.

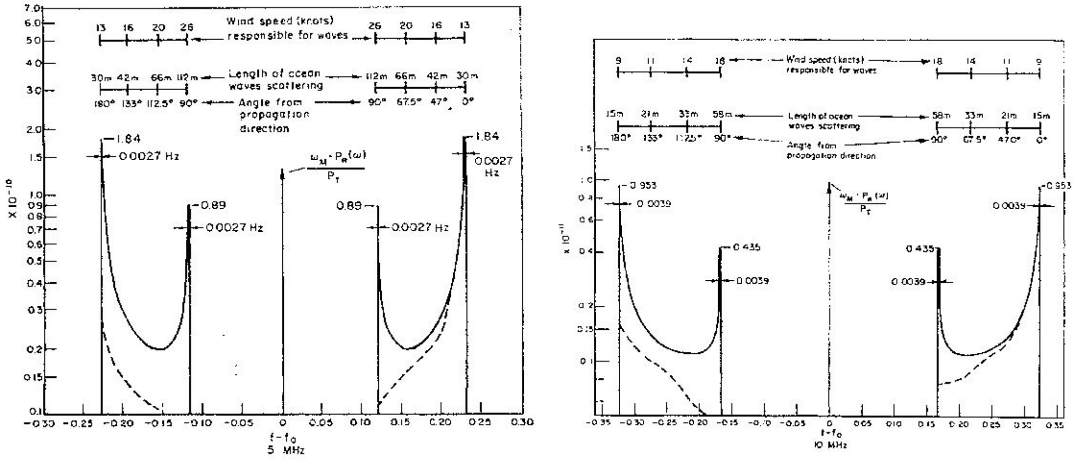

Figure 12.12 *Predicted received signal spectra for bistatic sea scatter of F12.9. Solid curves were computed for fully aroused Phillips isotropic ocean wave spectrum. Dashed curves represent expected measurements for non-isotropic sea. (a) 5 MHz carrier frequency. (b) 10 MHz carrier frequency.*

In practice, the received signal spectrum will be lower than that shown in (F12.12) for the semi-isotropic fully developed wind-wave model. The dashed curves show more typical shapes; the signal at the lower Doppler frequencies is likely to be weaker because the longer ocean waves responsible for their scatter are likely to be present less of the time.

Two groups have reported the results of such bistatic tests; in neither case were details of the ocean wave directional spectrum known with sufficient accuracy to allow complete quantitative comparisons. Wind and wave directions were available in an experiment reported by Barrick and Grimes (1970) at 5.8 MHz, permitting qualitative comparison and agreement; it will be described here. The other experiment was reported by Teague (1971) and Peterson, Teague, and Tyler (1970); using LORAN A signals (1.85 MHz), this experiment allowed the observation of quite long ocean waves (i.e., ~200 m wavelength), which are usually the essence of swell.

The experiment reported by Barrick and Grimes (1970) was conducted off Cape Kennedy, Florida, as shown in (F12.13). The transmitter was a buoy located 120 km from the receiving site on the coast. A binary phase-coded CW signal of basic interval 12.5μs was employed. The convolution of the signal with a replica of itself produces an effective pulse shape which is *not* uniform in amplitude over the 12.5 μs, as assumed in the example considered previously. Hence, the pattern of the illumination over the range gate one 12.5 μs interval behind the reception of the direct signal tapers in amplitude from a maximum at the center of the elliptical annulus shown in (F12.13) to zero at the baseline. Therefore, one would not expect to see the innermost "ears" or the sharp inner cutoff shown in (12.12) for a rectangular pulse. Also, the receiving antenna had a beamwidth of about 12°, pointing in the direction of the buoy (the transmitter antenna on the buoy was azimuthally isotropic). Hence, the antenna pattern tended to enhance scatter from the regions close to the baseline and behind the buoy with respect to scatter from regions toward the sides of the ellipse. The average transmitted power was 10 watts, and the spectral processor resolution was better than 0.01 Hz.

Shown in (F12.14) and (F12.15) are two observed spectra (non-averaged) at 5.8 MHz. Coast Guard wind and wave data was available for this area. On March 19, 1970, wind and relatively mild waves were from

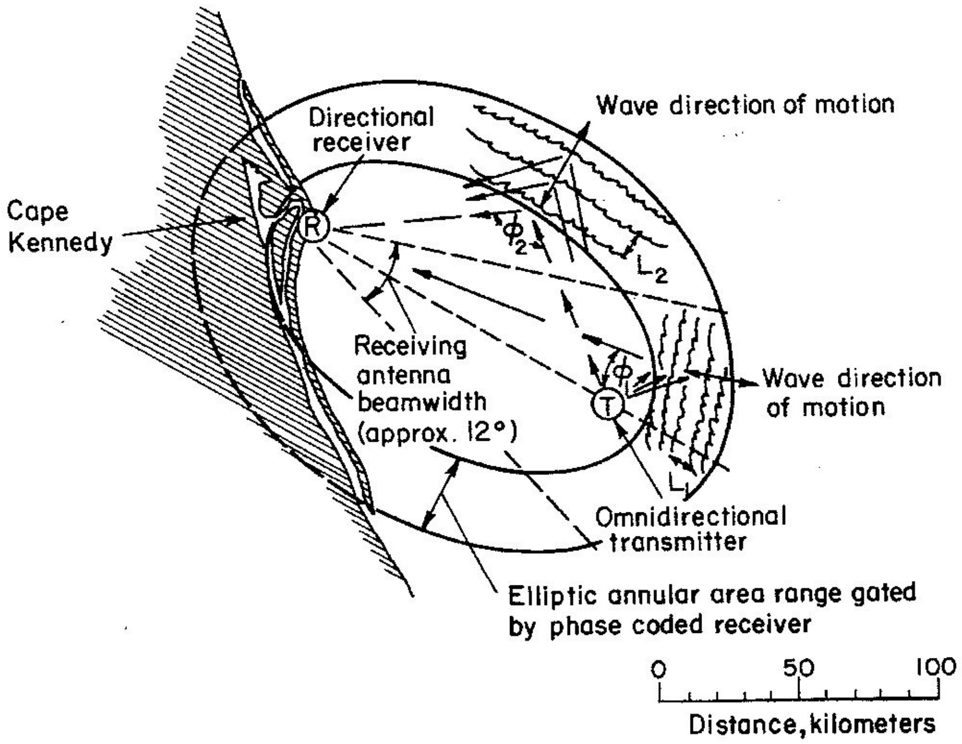

Figure 12.13 *Bistatic buoy-shore sea scatter configuration employed off Cape Kennedy.*

the east, as shown at the top of (F12.14). Thus one would expect approaching waves, predominantly from the region behind the buoy. Such waves approaching the buoy and baseline should produce positive Doppler shifts; such a spectral behavior was in fact observed, as shown at the bottom of (F12.14). On March 23, however, stronger, more variable winds blew from directions ranging between 220° and 315°. The "mean" wind and wave direction over that day was from the west, as shown at the top of (F12.15). Hence, strong negative Doppler shifts would be expected from the region behind the buoy. Again, this behavior was confirmed by the radar observations. Weaker positive Doppler shifts were produced by waves approaching the baseline, possibly near the receiving end of the path. It should be noted from these figures that the sea echoes fall within the bands predicted by the first-order Bragg-scatter theory. This represents a further confirmation of the theory and mechanism discussed here. Teague (1971) also observed that his echoes were always contained within the predicted "pedestal" region.†

12.2.4 Bistatic Surface-to-Satellite HF Experiment

As a final example of a remote sensing system based on first-order bistatic Bragg scatter, we examine an orbiting satellite receiver operating in conjunction with several ship or buoy transmitters. The geometry is shown in (F12.16). This concept was conceived and discussed by Barrick (1970), and is currently being developed by NASA into an experiment to be flown in the Skylab series of satellites (Ruck, et al., 1971). This experiment is capable of providing the directional waveheight spectrum (i.e., amplitudes and direction of ocean wave movements) near the transmitter; like preceding experiments, one must vary the transmitted frequency in some fashion over most of the lower HF band. Unlike previously

---

† The echo at zero Doppler shift is produced by land scatter behind the receiver, and also by some feed-through of the direct signal from the buoy.

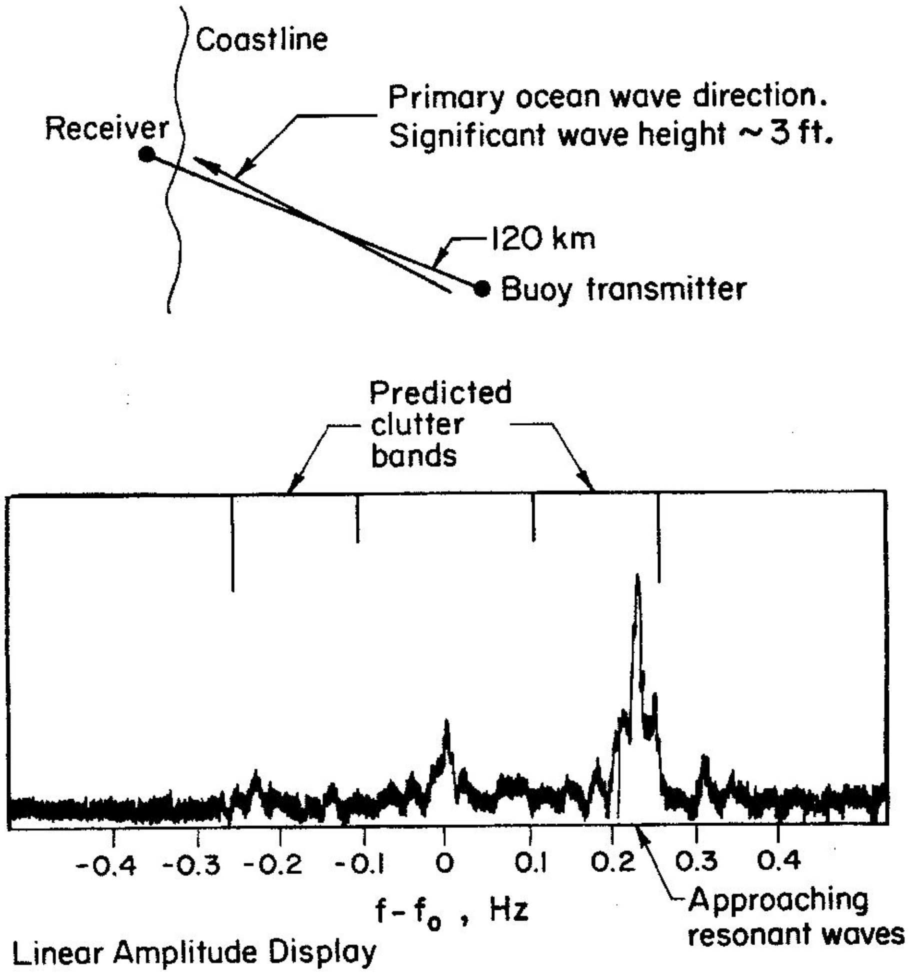

Figure 12.14 *Wind/wave directions and measured bistatic sea scatter Doppler spectrum at 5.8 MHz, 19 March 1970.*

discussed experiments, however, the receiver-processor need not be sensitive to the small Doppler shifts of the moving ocean waves, but rather obtains its directionality from the much larger Doppler shifts induced by satellite motion.

The transmitting antenna on the buoy or ship could consist of a simple vertical monopole (whip). The receiving antenna aboard the nonsynchronous satellite could be a pair of crossed loops or horizontal crossed dipoles. Short pulses (or equivalent coded signals) are employed. In general, ocean areas of constant time delay are represented by the intersection of confocal spheroids with the ocean surface; the foci of the spheroids are the transmitter and receiver points. The intersection curves on the surface are non-confocal ellipses. So as not to overcomplicate the mathematics, we consider here (for the sake of example) the case when the satellite is directly overhead, for then these elliptical annuli become circular annuli. The Doppler shift from each point on the ring due to satellite motion is different because of a varying overall range rate around the ring. Thus curves of constant Doppler shift are radial lines on the surface emanating from the transmitter. For the general case when the satellite is not directly overhead, these constant Doppler lines are hyperbolas intersecting the ellipses orthogonally; this case is analyzed in detail by Ruck et al. (1971).

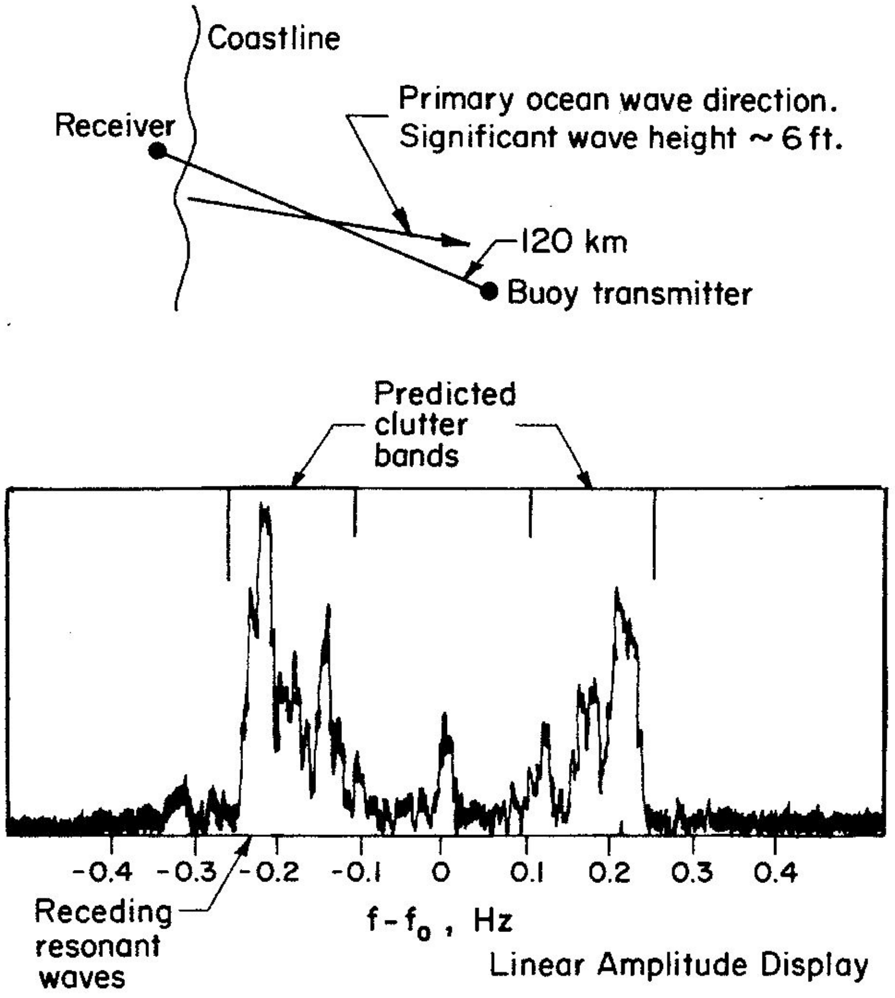

Figure 12.15 *Wind/wave directions and measured bistatic sea scatter Doppler spectrum at 5.8 MHz, 23 March 1970.*

In this case the bistatic angles to a point on the surface are $\theta_i = \pi/2$, $\theta_s = 0$. Hence the magnitude of the Bragg wavenumber of the scattering ocean waves is k_o here, rather than $2k_o$ for near-grazing backscatter configurations. We again intend to fix the wavenumber directions in the surface height spectrum to the space around the buoy or ship, since the original scattering cross sections (12:20) were defined with respect to the local incidence directions at each point on the scattering ring. Hence we take the x-axis and κ_x direction as the horizontal line within the orbital plane. Thus the satellite-induced Doppler shift to any point on the ring of radius R_T at an angle φ with respect to the +x-axis is $\omega_o v_s(R_T/R_R) \cos\varphi/c = \omega_{dm} \cos\varphi$, where here the maximum Doppler is $\omega_{dm} = \omega_o v_s(R_T/R_R)/c$, v_s being the velocity of the satellite, ω_o the radian carrier frequency, and c the free space radio wave velocity. Using (12:20) in (12:19), the average received one-sided power spectrum for a patch on the ring ($dS = R_T \Delta R_T \Delta\varphi$) is found to be:

$$dP_R(\omega) = \frac{4P_T G_T G_R F_T^2 \Delta R_T \Delta\varphi}{k_o^2 R_T R_R^2} S(k_o \cos\varphi, k_o \sin\varphi)\delta(\omega - \omega_o \pm \omega_+ - \omega_{dm} \cos\varphi) . \qquad (12:29)$$

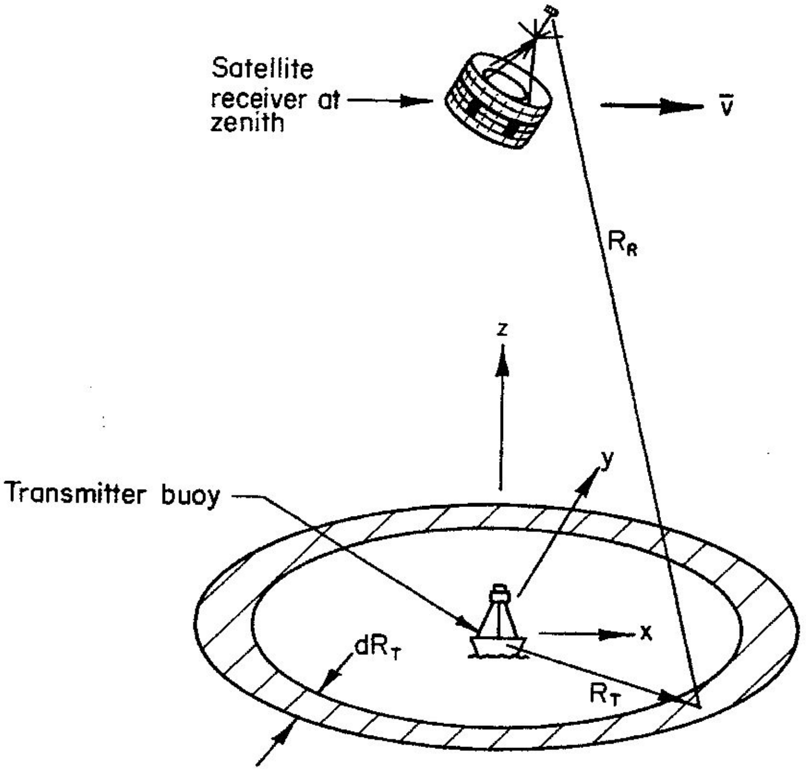

Figure 12.16 *Bistatic HF surface-to-satellite radar.*

Here the width of the ring, ΔR_T is related to the effective signal pulse width, τ, as $\Delta R_T = c\tau$. The direct signal from the transmitter to the satellite is observed at a delay $t_d \simeq R_R/c$ (for $R_R >> R_T$); hence the range R_T is given in terms of time delay $t = (R_R + R_T)/c$ as $R_T \simeq ct - ct_d$.

In a manner similar to that following (12:25), we integrate (12:29) over φ to obtain the total signal spectrum from the range ring. The various factors preceding S in the above equation are assumed to be constant in this integration. As before, we assume that the sea height spectrum is homogeneous over the circle around the transmitter. Then we obtain an expression for the directional waveheight spectrum of the surface in terms of the received signal spectrum as follows:

$$S' k_o \eta/\omega_{dm}, k_o \sqrt{1 - \eta^2/\omega_{dm}^2} = \frac{R_T R_R^2 k_o^2}{4 \Delta R_T G_T G_R F_T^2} \sqrt{\omega_{dm}^2 - \eta^2} \times \frac{P_R(\omega)}{P_T}, \tag{12:30}$$

where $\eta = \omega - \omega_o \mp \sqrt{gk_o}$. Normally, satellite-induced Doppler is so great that ocean-wave-induced Doppler can be neglected ($\omega_{dm} >> \sqrt{gk_o}$); in this case, $\eta \simeq \omega - \omega_o$. Thus by measuring the received sea echo signal spectrum at the satellite, and knowing its velocity, position, and orbital plane, one can obtain the directional waveheight spectrum for spatial wavenumbers $\kappa_x = k_o \cos\varphi$, $\kappa_y = k_o \sin\varphi$, for all φ by noting that $\cos\varphi = \eta/\omega_{dm}$ and $\sin\varphi = \sqrt{1 - \eta^2/\omega_{dm}^2}$. One must vary the carrier frequency, however, to sample the spectrum at a different *total* wavenumber, κ ($\kappa = \sqrt{\kappa_x^2 + \kappa_y^2} = k_o$). As before, there is an ambiguity, in that waves crossing the circle at $+\varphi$ cannot be distinguished from waves crossing the circle at $-\varphi$. Ruck et al. (1971) discuss several techniques for removing this ambiguity.

As an illustration of what the received signal spectrum will look like at 5 and 10 MHz for fully developed semi-isotropic waves describable by the Phillips spectrum (12:13), we consider the following example. The antenna on the satellite is assumed to be a half-wave dipole with gain 1.64, and the "free-space" gain of the quarter-wave monopole transmitting antenna is taken to be 0.82. The satellite is at an altitude of 300 km and moving with velocity 8000 m/s. We select a pulse length τ = 10 μs, yielding a clutter ring width $\Delta R_T = 3$ km. Let us select a time delay $t - t_d = 50\ \mu s$, corresponding to $R_T = 15$ km. Then we obtain the spectra shown in (F12.17). At the top of these plots, the angle φ of ocean wave directions producing the echo at that Doppler shift is given. The maximum Doppler shift from the satellite is $f_{dm} \simeq 6.67$ Hz at 5 MHz, which is considerably larger than the ocean-wave Doppler $\sqrt{gk_o}$ of 0.161 Hz; hence the neglect of ocean-wave-induced Doppler shifts in this experiment seems reasonable. Also, there is no need for spectral processing resolution less than about 0.5 Hz, which alleviates the data handling requirements aboard the satellite.

The satellite should receive and process the direct signal as well as the sea-reflected signal. The direct signal will serve (a) as a time reference, (b) as a Doppler (frequency) reference, and (c) to calibrate and remove any unknown path loss through the ionosphere from the sea return. For the example considered in the preceding paragraph, the direct signal power received at the satellite is of the order of 10^{-9} P_T to 10^{-11} P_T, depending upon the gain pattern of the transmitting antenna in the direction of the satellite. This compares with a total maximum received sea echo power of approximately 2.5×10^{-12} P_T at 5 MHz.

The most serious limitations on a system such as this are imposed by the ionosphere. Orbital altitudes greater than 200 km will often not allow penetration of the lower HF frequencies through the ionosphere to the satellite. The F2 layer of the ionosphere is the densest and if the satellite is orbiting above it (i.e., above 300 km), then the following conclusions concerning ionospheric limitations were determined by Ruck et al. (1971).

(a) The operating frequency of the sensor must be confined to the range 3.5 to 30 MHz. (This permits sensing of ocean waves with lengths between 10 and 100 m.) Propagation conditions favorable to the system exist at night between 0 and 6 hr local time. At such times the minimum ionospheric penetration frequency ranges from 3.5 to 5 MHz depending upon the season and sunspot cycle. Operation throughout the rest of the day can take place at frequencies as low as 9-10 MHz.

Restriction of operation at the lowest frequencies to a six-hour period every day, however, may not limit the utility of the sensor for the following reason. At the lowest frequencies, the longest ocean waves are being observed (i.e., greater than 40 m). However, these longer ocean waves require greater times (i.e., of the order of 24 h) to build up and die down (T12.1). Thus the heights of these longer waves will not change appreciably over times less than a day, and their observation once a day should be sufficient.

(b) During normal ionospheric conditions, the (excess) absorption loss due to passage through the ionosphere will be less than approximately 15 dB providing the operating frequency exceeds the minimum penetration frequency by 0.5 MHz.

(c) The noise environment encountered by the satellite will be that due to cosmic noise, with a maximum effective noise temperature of about 4×10^{6} °K at 3 MHz.

Based on these loss and noise considerations, the study concludes that adequate signal-to-noise ratios can be obtained with average transmitter power output levels of the order of 10 W for a satellite in a 400 km orbit.

12.3 Second-Order HF Sea Echo

It was noted several places previously in this chapter (when comparing the first-order Bragg scatter theory with measured sea echo spectra) that the observed records often contain smaller—but non-negligible—peaks at Dopplers other than the first-order lines. Also, Barnum (1971) observes an overall higher "floor" under the sea spectra than would be expected from normal processor and noise clutter. He has confirmed that this "floor" is produced by sea echo by (a) looking at land scatter for comparison, and (b) shutting off the transmitter and observing the "floor" due to system and external noise. This "floor" and the higher-order peaks are not predicted from the first-order theory developed previously; one must go to a higher-order

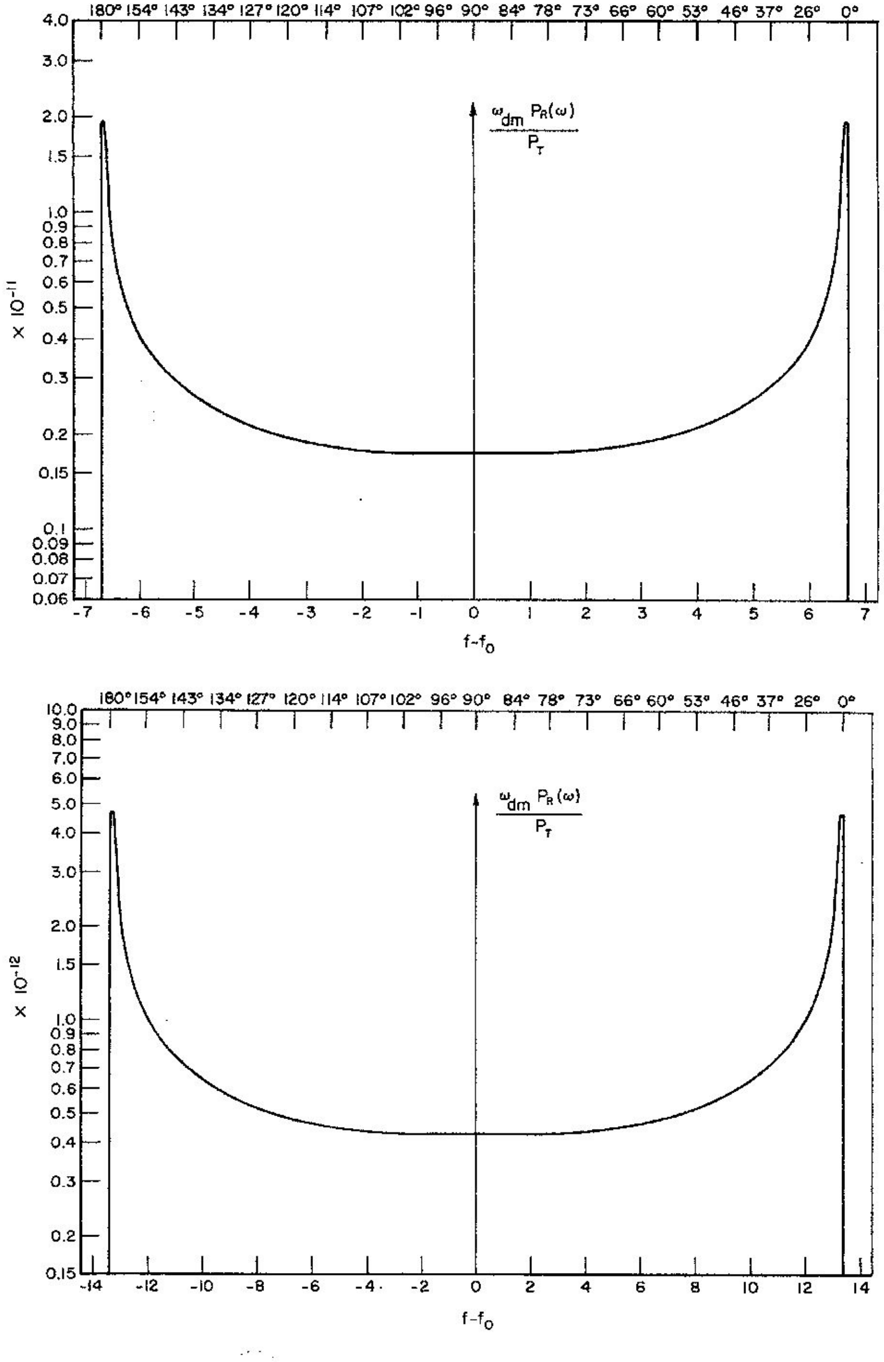

Figure 12.17 *Predicted received signal spectra for bistatic sea scatter of F12.16; computed for fully aroused Phillips isotropic waveheight spectrum (a) 5 MHz carrier frequency (b) 10 MHz carrier frequency.*

analysis of scattering and ocean wave interaction processes. Such spectral contributions could ultimately pose a limitation on the performance of any radar system designed for first-order Bragg scatter, and hence they should be qualitatively and quantitatively understood.

A more positive reason for examining these higher order sea echo spectral contributions is that they may in themselves provide additional information about the state of the sea. This suggestion was made by Hasselmann (1971), Crombie (1971), and Barrick (1971b).

Two obvious sources for this higher-order return suggest themselves: (a) the second-order terms for scatter from the Rice boundary perturbation theory, and (b) the second-order terms from the hydrodynamic equations describing the water surface height. To simplify matters here, we consider backscattering at grazing incidence with vertical polarization over a perfectly conducting sea. Then it can be shown that the average second-order backscatter cross section per unit surface area per rad/s bandwith, $\sigma_{VV}(\omega)$, to be used with (12:19) is:

$$\sigma_{VV}(\omega) = 16\pi k_o^4 \iint_{-\infty}^{\infty} \left|\Gamma_T(\vec{\kappa}_1,\vec{\kappa}_2)\right|^2 \delta(\eta - \omega_1 - \omega_2) W(\vec{\kappa}_1) W(\vec{\kappa}_2)\, dpdq \,, \tag{12:31}$$

where $\vec{\kappa}_1 = (p - k_o)\hat{x} + q\hat{y}$: $\vec{\kappa}_2 = -(p + k_o)\hat{x} - q\hat{y}$; $\kappa_1 = |\vec{\kappa}_1|$; $\kappa_2 = |\vec{\kappa}_2|$; $\omega_1 = \text{sgn}\,(\kappa_{1x})\sqrt{g\kappa_1}$; $\omega_2 = \text{sgn}\,(\kappa_{2x})$ $\sqrt{g\kappa_2}$; $\eta = \omega - \omega_o$ is the Doppler shift from the carrier; $\delta(x)$ is the Dirac impulse function of argument x; and $W(\vec{\kappa}) \equiv W(\kappa_x,\kappa_y)$ is the directional spatial waveheight spectrum of the ocean, as defined in (12:21).

For the second-order electromagnetic contributions alone, Γ is found to be

$$\Gamma_{EM} = \frac{1}{2}\, (\kappa_{1x}\kappa_{2x} - 2\vec{\kappa}_1 \cdot \vec{\kappa}_2)/\left(\sqrt{\vec{\kappa}_1 \cdot \vec{\kappa}_2} + k_o\Delta\right), \tag{12:32}$$

where Δ is the normalized impedance of the sea surface, as discussed by Barrick (1971a).

The second-order hydrodynamic effects produce

$$\Gamma_H = -\frac{i}{2}\left[\kappa_1 + \kappa_2 + \left(\kappa_1\kappa_2 - \vec{\kappa}_1 \cdot \vec{\kappa}_2\right)\left(1 - 2\eta^2/\left(\eta^2 - \omega_B{}^2\right)\right)(g/\omega_1\omega_2)\right], \tag{12:33}$$

where $i = \sqrt{-1}$ and $\omega_B = \sqrt{2gk_o}$ is the first-order Bragg Doppler shift. The total Γ_T which must be used in the integral to account for both types of second-order effects is

$$\Gamma_T = \Gamma_{EM} + \Gamma_H \tag{12:34}$$

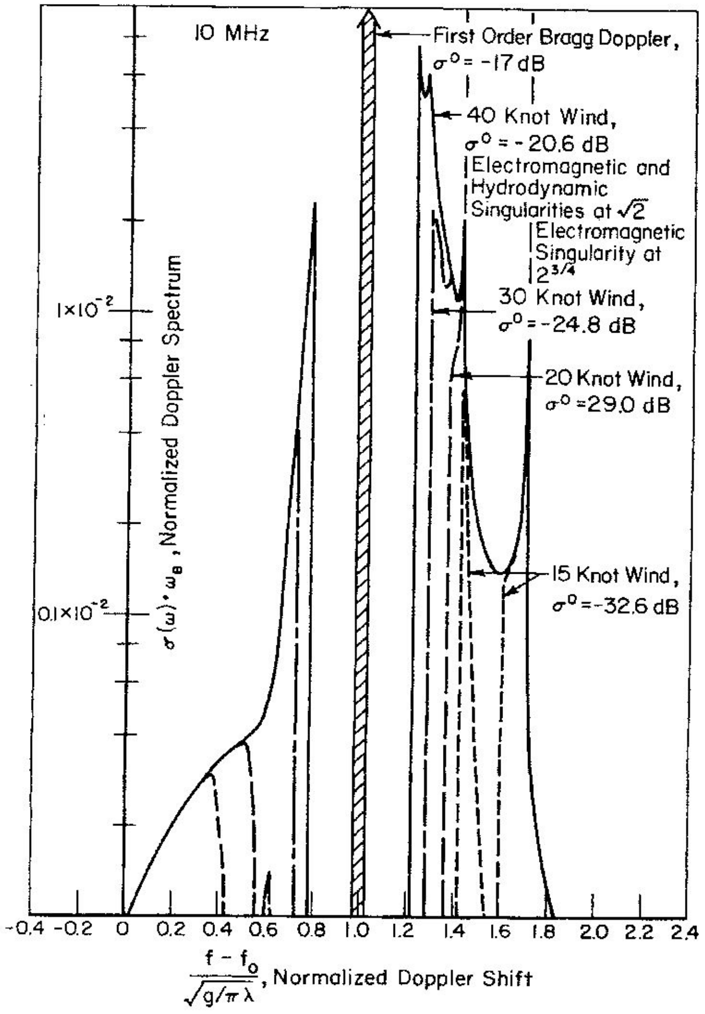

Figure 12.18 *Predicted Doppler spectrum of first and second-order near-grazing sea backscatter at 10 MHz for propagation in upwind direction (Phillips semi-isotropic waveheight spectrum assumed).*

The above integral clearly shows that a double-scatter Bragg process is responsible for the second-order sea return. The scattered radio wavenumber, $-k_0\hat{x}$, is equal to $\vec{\kappa}_1 + \vec{\kappa}_2 + k_0\hat{x}$, where the last term is the incident radio wavenumber. The frequency, ω, of the scattered field is identically $\omega_1 + \omega_2 + \omega_0$. In the case of the electromagnetic second-order effects, an ocean wavetrain with wavenumber $\vec{\kappa}_1$ scatters the radio energy along the surface to a second wavetrain with wavenumber $\vec{\kappa}_2$, which redirects it back toward the source; the intermediate radio wave can be either propagating or evanescent. In the case of the hydrodynamic effects, two ocean wavetrains produce second-order ocean waves with wavenumbers $\vec{\kappa}_1 \pm \vec{\kappa}_2$; these latter ocean waves are not freely propagating because they do not satisfy the first-order gravity wave dispersion relationship, but they do produce radar scatter.†

---

† One of the two integration processes can be done in closed form, this resulting from the impulse-function occurring in the integrand. The remaining integration is done numerically because of the complex form of the integrand.

To illustrate the nature of both of these second-order effects at HF, we perform the integration indicated in (12:31) numerically† for the following example. The frequency chosen is 10 MHz, and we employ the Phillips semi-isotropic wind-wave model of (12:13) for $W(\vec{\kappa})$, the first-order waveheight spectrum. Using different windspeeds as the parameter and considering propagation in both the upwind and crosswind directions, we obtain plots shown in (F12.18) and (F12.19) for the signal spectrum $\sigma_{VV}(\omega)\omega_B$. The first-order discrete Doppler lines are also shown for reference; they will be present at 10 MHz for the Phillips model at winds greater than 9-1/2 knots. Also shown is the normalized radar cross section for each spectrum, $\sigma^O_{VV}(\sigma^O_{VV} = \frac{1}{2}\int_{-\infty}^{\infty} \sigma_{VV}(\omega)d\omega)$, where the spectra plotted here are two-sided, i.e., $\sigma^O_{VV}(-\omega) = \sigma^O_{VV}(\omega)$.

The figures illustrate that second-order continuous Doppler sidebands do occur and their magnitude will depend upon sea state. These sidebands contain continuous, integrable singularities (of the square-root-types) at positions of $\sqrt{2}$ and $2^{3/4}$ times the first-order Bragg line. The $\sqrt{2}$ singularity is due to both electromagnetic and hydrodynamic second-order effects. Electromagnetically, it is due to higher-order Bragg scatter, i.e., from ocean waves of length $L = \lambda$ (rather than $\lambda/2$). These ocean waves travel at a speed $\sqrt{2}$ greater than those at $\lambda/2$, and hence the $\sqrt{2}$ spike; this is a "grating lobe" effect occurring for larger diffraction grating spacings. Hydrodynamically, the $\sqrt{2}$ singularity is due to the second spatial harmonic of the trochoidal wave profile of fundamental length $L = \lambda$; this second harmonic is of length $\lambda/2$, producing first-order Bragg scatter, but it travels at the same phase speed as the fundamental to which it is attached. The phase speed of the fundamental is $\sqrt{2}$ greater than the normal ocean wave with length $\lambda/2$, and hence the $\sqrt{2}$ hydrodynamic contribution. Finally, the $2^{3/4}$ singularity is due to a "corner reflector" electromagnetic effect. This occurs when the two sets of (non-evanescent) scattering ocean waves pass through 45° with respect to the propagation direction. The total Doppler shift from these two sets of ocean waves, $\omega_1 + \omega_2 = \omega_B(\sqrt{\cos\alpha} + \sqrt{\sin\alpha})$, is maximum† at $\alpha = 45°$, i.e., $2^{3/4}\ \omega_B$. Thus a condition of mathematical stationarity occurs for the Doppler shift when α passes through 45°.

As deduced previously from (F12.18) and (F12.19), the second-order received sea echo spectrum increases both in its amplitude and in its proximity to the first-order Bragg lines with increasing wind speed. Conversely, for a given wind speed, the same second-order spectrum increases with increasing carrier frequency. The common parameter for each curve in the figures is $g/(2k_Ou^2)$, where u is the wind speed and k_O $(= 2\pi f_O/c)$ is the radar wavenumber. Thus for a given value of this parameter, the same spectrum curve can be obtained by doubling wind speed and reducing frequency by a factor of four, or if the frequency is increased by a factor of four, by halving the wind speed.

At present, we have no conclusive experimental validation of the theory because of a general lack of accurate HF sea echo spectrum measurements. Several available records, however, exhibit many of the principal features of our predicted second-order spectra. Crombie's ground-wave measurements at 8.37 MHz (F12.5) shows a definite second peak above the positive first-order line; its position is greater than the first-order line by a factor of 1.36. From (F12.18), this would correspond to seas aroused by a wind speed of about 21-22 knots. Also evident in this record by Crombie is a third peak which occurs at about 1.69 times the first-order line; the $2^{3/4}$ (= 1.682) singularity appears to explain this peak. Barnum's sky-wave backscatter measurements (F12.8) at 25.75 MHz also appear to contain higher-order peaks beyond the first-order line. He estimates that these occur at 1.35, 1.70, and 2.00 times the first-order line. Again, the first higher order peak at 1.35 is explainable by seas driven by about 13-knot winds, while the second peak is quite close to the predicted $2^{3/4}$ singularity. As with Crombie's record, the height of the third peak near $2^{3/4}$ is less than that of the second, while the height of the second is considerably less than that of the first-order Bragg line; these features all agree with the predicted second-order spectral behavior.

Hasselmann (1971) has suggested (based upon several approximations which were examined in detail by Stewart (1971)) that the second-order sea echo spectra above and below the first-order Bragg lines should be symmetric reproductions of the first-order temporal nondirectional waveheight spectrum of the sea, centered about the first-order lines. Our more detailed derivations show that these second-order spectra are *not* symmetric about the Bragg lines; this is especially true for the crosswind case, where no energy at all appeared above the Bragg line. However, these second-order contributions do possess *some* of the features of the first-order waveheight temporal spectrum centered around the Bragg lines. For example, they become higher in

---

† The angle α here is $(180° - \phi)/2$, where ϕ is the bistatic angle between the incident and the first-scattered radio wave. Backscatter produced by such a double interaction process requires that the bistatic angle between the first-scattered and second-scattered (i.e., backscattered) radio wave be ϕ.

amplitude and move in closer to the Bragg lines with increasing wind speed and/or frequency. Hence we agree with Hasselmann's basic conclusions that sea state *can* be deduced at higher HF frequencies by examining the features (i.e., strength and position) of the second-order peaks in the sea echo backscatter spectrum. Upon further confirmation by measurements, this technique may prove to be quite valuable in remote sensing of sea state, especially with ionospheric radars which are restricted in their operation to the upper HF region.

12.4 UHF Indirect Bragg Scatter Using Two Frequencies

A technique currently under development for measuring the slope spectrum of the longer gravity waves will be briefly examined here. This concept employs the correlation between the sea return at two closely spaced UHF frequencies as a measure of the larger and longer ocean waves present. The interpretation of the final result of the derivation shows that the mechanism yielding the slope spectrum of the surface *resembles* Bragg scatter; the surface slope spectrum is evaluated, however, not at the wavenumber corresponding to the carrier frequency, but at the "beat" wavenumber corresponding to the difference between the two UHF frequencies.

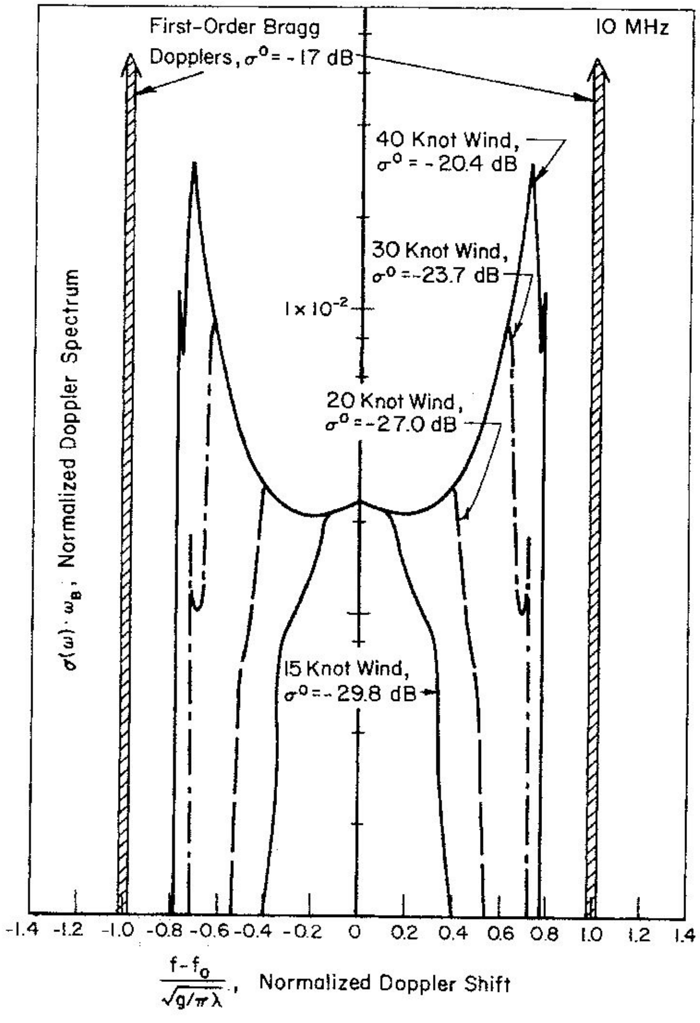

Figure 12.19 *Predicted Doppler spectrum of first and second-order near-grazing sea backscatter at 10 MHz for propagation in crosswind direction (Phillips semi-isotropic waveheight spectrum assumed).*

Before summarizing the analysis, let us briefly discuss the physics behind the anticipated behavior. HF scatter from the sea has been conclusively shown, both theoretically and experimentally, to be due to the Bragg (or diffraction grating) effect. The theory shows that a *mathematical* upper limit of frequency (for a given waveheight) can be expected, beyond which the perturbation approach used should not be valid; this upper frequency in terms of wind speed is given in (F12.6). Several recent experimental efforts, however, have established that the Bragg mechanism produces non-specular sea scatter at UHF, microwave, and even millimeter-wave frequencies. Wright (1968) deduced this from his signal spectra—as well as from quantitative comparisons of σ^o for various polarizations with the previously developed theory; he observed scatter from waves generated in a controlled wind tank. Guinard and Daley (1970) established that the Bragg mechanism also explained—even quantitatively—the microwave scatter they observed on the sea. In the latter case, much larger and longer ocean waves are present; yet measurements have confirmed that the much smaller wavelets actually producing microwave backscatter are those whose lengths are $\lambda/(2 \sin \theta)$, where θ is the angle of incidence from the vertical. Again, their results measured for σ^o_{vv} and σ^o_{hh} (the average backscatter cross sections per unit area) agree quantitatively with theoretical predictions based on a *slightly* rough surface, i.e., (12:20), (12:22), and (12:23), in their dependence on polarization, incidence angle, and saturation effect in the wind-wave equilibrium region. Such agreement is apparent over most aspect angles, as long as one stays away from the specular direction (i.e., the vertical for backscatter) and grazing incidence (where shadowing becomes significant).

Barrick and Peake (1968) and Wright (1968) explained this behavior by considering the surface at these higher frequencies to be a "composite", made up of two or more scales of roughness. Thus, one has the Bragg-scattering wavelets riding on top of the longer and higher gravity waves. With this model, one obtains two regions of scatter: the quasi-specular region and the diffuse region. Near the specular direction, backscatter is produced via reflections from many specular points, or facets, oriented normal to the line of sight. For the sea, this type of backscatter dominates out to 10-15° from the vertical; its magnitude and behavior is predictable from both physical and geometrical optics approaches. Farther away from the specular direction, scatter is predictable via the Bragg mechanism, as though the smaller wavelets riding on the larger waves were really the only ones present. The magnitude and polarization dependence of this "diffuse" scatter follows (12:20) for the slightly rough surface.

Valenzuela (1968) first noted that the magnitude of the return from a slightly rough surface (i.e., the Bragg scatter) does have some dependence upon the local incidence and scattering angles, as seen in (12:20)—even though the dependence may be weak for some polarization states over a large range of angles. Hence the effect of the longer gravity waves under the Bragg-scattering wavelets should be seen as a "tilting plane", modulating the amplitude of the Bragg scatter because of the slope of the larger-scale wave underneath. Let us take as an example a uniform Bragg-scattering wavetrain on top of a single larger and longer sinusoidal wave. Now imagine a short radar pulse, less in its spatial length than one-quarter the wavelength of the longer sea wave, propagating along the surface and backscattering via the Bragg mechanism from the wavelets. Due to the slope of the longer sinusoidal wave and hence the periodic variation of the local angle of incidence to the pulse as it propagates along, the radar receiver should see a return which is amplitude modulated in a periodic manner by the longer gravity wave. If one analyzed the spectrum of this amplitude modulated signal, he would be able to relate the result to the slope of the larger wave at its own spatial frequency or wavenumber. Thus one could, with such a short-pulse experiment, measure the slope spectrum of the longer gravity waves by Fourier transforming the received signal strength and looking at its spectrum. This technique was examined recently by Soviet investigators (Zamarayev and Kalmykov, 1969).

The concept to be analyzed here is quite similar to that described above. By using two frequencies, however, and cross-correlating their received powers, one eliminates the Fourier transform process required for the short-pulse technique. Nearly CW signals can be used. The bandwidth required (i.e., frequency separation here) is much the same as for the short-pulse, however, because both techniques are essentially employing spatial range resolution to distinguish the slopes of the underlying longer gravity waves. By eliminating the spectral analysis process and the short pulse requirement, we feel that the two-frequency correlation concept offers a possibly more tractable sensing tool.

The two-frequency correlation concept was analyzed in Ruck et al., (1971) in detail. The derivation there was meant to establish quantitatively some of the features of the correlated power. To facilitate the analysis, the following assumptions were imposed: (a) Only backscatter was considered. (b) The surface was taken as perfectly conducting. (c) Horizontal polarization was examined for incidence and backscatter. (d) A

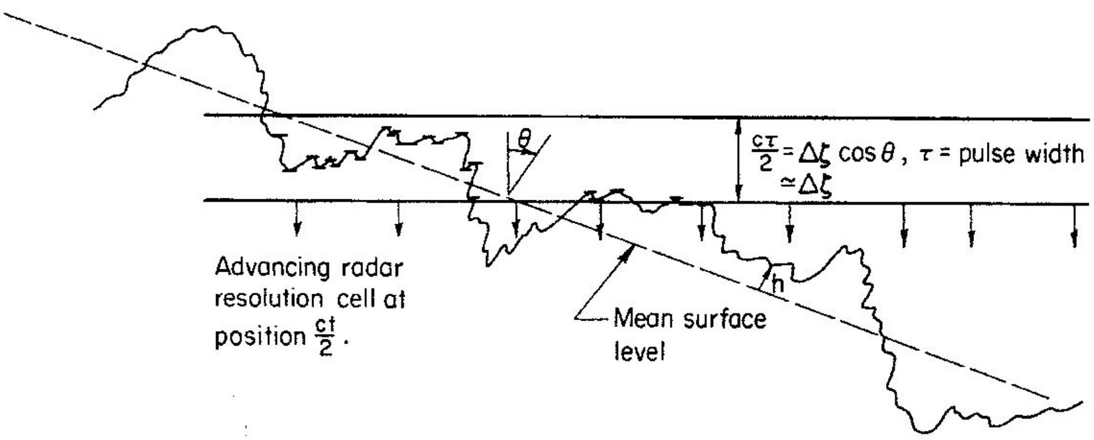

Figure 12.20 *Physical picture of specular point scatter. Specular points within radar resolution cell are shown highlighted.*

one-dimensional random surface was analyzed, corrugated along the plane of incidence. (e) The incidence angle region was selected to be not too close to the specular direction (i.e., the vertical), but yet not so close to grazing that shadowing is a problem. (f) The slopes of both the large-scale and small-scale sea-wave components present were assumed small.

Based upon these assumptions, the variance of the backscattered power densities at two frequencies, f_b and f_a, was obtained, i.e., $\mathrm{Var}[P(\Delta k)] \equiv \langle P_a P_b \rangle - \langle P_a \rangle \langle P_b \rangle$, where $\Delta k = k_b - k_a = 2\pi(f_b - f_a)/c$. Thus, Δk can be considered a "beat" or difference wavenumber. The length and width of the surface patch (assumed square) subtended in the radar cell is L, and the angle of incidence from the vertical is θ. Then the result for the variance was found to be

$$\mathrm{Var}[P(\Delta k)] = \frac{k_a^2 k_b^2 L^6 E_0^4}{Z_0^2 q_z^2 16\pi^2 R_0^4} \left\{ \left[\frac{\sin(\Delta k L \sin\theta)}{\Delta k L \sin\theta} \right]^2 \left[f^2(k_0\xi) W(k_0\xi) \right]_{s=0}^2 \right.$$
$$\left. + \left[\frac{d(f^2(k_0\xi)W(k_0\xi))}{ds} \right]_{s=0}^2 \cdot \frac{1}{\pi L} W_{SL}(2\Delta k \sin\theta) \right\}, \qquad (12:35)$$

where R_0 is the distance from the scattering patch to the far-field point, E_0 is the electric field strength of the plane wave incident on the surface, and Z_0 is the free-space wave impedance. The quantity $W(\kappa_x)$ is the one-dimensional spatial waveheight spectrum of the sea surface in the wave-length range around one meter; $W_{SL}(\kappa_x)$ is the one-dimensional spatial waveslope spectrum of the larger gravity waves. The remaining quantities appearing in (12:35) are $q_z = 2\cos\theta$, $s = d\zeta_L/dx$ = slope of the larger-scale component of the surface, $\xi = 2s\cos\theta - 2\sin\theta$, and $f(k_0\xi) = k_0\,[\sqrt{1 - (2s\cos\theta - \sin\theta)^2} + \cos\theta + s\sin\theta] \times [\cos\theta + s\sin\theta]$.

In order to obtain numerical estimates of the relative magnitudes of the first and second terms in (12:35), we must evaluate the quantity in square brackets and its derivative at zero slope. To do this, a form for the waveheight spectrum of the smaller-scale (Bragg-scattering) ocean waves must be assumed. By selecting our operating frequency in the UHF band (viz., near 1 GHz), we ensure that these Bragg-scattering ocean waves are of the order of 30 cm in length. Such waves are still gravity waves (in contrast to capillary waves) and hence should follow the Phillips model in the saturation region. Furthermore, these shorter gravity waves require winds greater than only 1-1/2 knots to excite them; hence, they are nearly always present. On the other hand, their build-up time is of the order of 10 minutes, in contrast to capillary waves which build up and die down in a matter of seconds; therefore they should exist rather uniformly and stably over times and areas which are significant in making the measurements. This is the reason that 1 GHz is proposed as the operating frequency.

One can readily convert the two-dimensional Phillips model (12:13) to a one-dimensional version. The result is

$$W(\kappa_x) = \frac{B}{\kappa_x{}^3}\ , \tag{12:36}$$

where $\kappa_x > 0$ (i.e., the above spectrum is one-sided), and as before, B = 0.005 (dimensionless).

Upon evaluation of the indicated factors in (12:35), we obtain

$$\mathrm{Var}[P(\Delta k)] = \frac{k_a k_b L^6 B^2 E_0^4 \cot^6\theta}{Z_0^2 2^6 \pi^2 R_0^4} \left\{ \cos^2\theta \left[\frac{\sin(\Delta k L \sin\theta)}{\Delta k L \sin\theta}\right]^2 + \frac{(5\sin^2\theta - 3\cos^2\theta)^2}{\pi L \sin^2\theta} W_{SL}(2\Delta k \sin\theta) \right\}. \tag{12:37}$$

Let us now interpret the two terms in (12:35) and (12:37). The first term is merely the Fourier transform of the range resolution cell illumination pattern on the surface (i.e., here we assumed uniform illumination over the cell of length $(L/2)\sin\theta$) evaluated at spatial frequency $2\Delta k$. If the range cell is beam-limited rather than pulse-limited, one might approximate the cell illumination by a uniform pattern between the half-power points of the antenna beam pattern on the surface. If one uses a more realistic illumination pattern along this cell, the (sin x)/x function will be replaced by the Fourier transform of the actual pattern. With a properly selected and tapered illumination function, the first term can be kept very small, so long as $\Delta kL \sin\theta$ is large compared to unity. In a pulse-limited situation, this means making the pulse length, τ, sufficiently long that $2\pi\Delta f\tau \sin\theta >> 1$ over the range of Δf used in the experiment.

The second term in (12:35) and (12:37) contains the desired information about sea state, as represented in the waveslope spectrum of the longer gravity waves. Their waveheight spectrum is readily related to $W_{SL}(\kappa_x)$ as $W_{HL}(\kappa_x) = W_{SL}(\kappa_x)/\kappa_x^2$. Hence, measurement of the waveslope spectrum by sweeping frequency (and thus varying Δk) can be directly transformed into waveheight spectral information. It is desirable to select θ, the incidence angle, so that the magnitude of the second term is enhanced with respect to the first. For horizontal polarization and backscatter, a poor choice would be θ at or near 37.8° from the vertical, for this makes the factor in parentheses multiplying the second term identically zero. On the other hand, a value of θ near 60° will usually result in the second term being larger than the first for W_{SL} non-zero and near its equilibrium (saturation) value.

The argument of the term containing the waveslope spectrum would lead one to think that a Bragg-effect scatter were occurring at the beat wavenumber $2\Delta k \sin\theta$, rather than at the carrier wavenumber k_a or k_b. Hence we refer to this as an indirect Bragg-scatter measurement. By sweeping Δf from 2-20 MHz, one should be able to obtain sea state information by measuring the magnitude, shape, and cutoff of the larger gravity wave slope spectrum. The two frequencies can be generated quite simply by using a balanced modulator near the output of the transmitter. Since the scattered *power* is correlated in the receiver, it is not necessary to maintain phase coherence of the two signals through the receiver channels. Hence the equipment requirements should present no significant obstacles.

This technique, examined here for backscatter and horizontal polarization, can be used for other polarization states and in bistatic arrangements (so long as one avoids the specular reflection direction). The analysis is currently being extended to include three-dimensional scatter from two-dimensionally rough, non-perfectly conducting surfaces. The basic nature of the results are not expected to differ from those examined here, however. Up to the present, this technique has not been tested experimentally; hence we can offer no measured data for validation of the concept. Plans are underway to test the technique in the near future.

12.5 Sea State Effects on a Microwave Radar Altimeter Pulse

As a final tool for remote sensing of both geodetic and sea state information, we discuss the microwave radar altimeter. Decisions by NASA to fly short-pulse altimeters in both the GEOS-C and Skylab series of satellites have recently accelerated theoretical and experimental efforts on radar altimetry. A sufficiently clear picture is presently available—both from analysis and experimental data—of the basic interaction process between the pulse and the sea surface. At and near the (vertical) sub-altimeter point, microwave scatter is produced by specular points which are distributed in height, thus having some obvious relationship to sea state. In most cases of interest, the effective radar spatial pulse width is smaller than the ocean waveheights it encounters on the surface; hence a stretching of the pulse will occur due to sea state. When the purpose of the experiment is to find the instantaneous mean sea level (for geodetic reasons) to an accuracy of less than one meter, one is faced with the problem of finding this position in a received echo distorted by sea state effects; hence one must remove such effects from the signal. On the other hand, one may wish to use the radar altimeter as a sea state sensor; in this case, he would like to know how to relate sea state to the received pulse distortion. Both problems are examined here.

The first subsection discusses the specular point-theory of sea scatter and obtains the distribution of these points as a function of waveheight. The second subsection then applies the specular-point scattering model to the radar altimeter configuration and determines a simple closed-form solution for the altimeter return for the case of Gaussian pulse and beam widths. The final subsection simplifies this result for certain limiting altimeter configurations commonly used in practice, and compares the model with measured data.

12.5.1 Specular Point Distribution and the Scattering Model

For the microwave frequencies at which an altimeter will operate, scatter from the sea within the near-vertical region directly beneath the altimeter is quasi-specular in nature. This means that backscatter is produced by specular or glitter points on the surface whose normals point toward the radar. Such scatter persists only to about 10-15° away from the vertical, since gravity waves can seldom maintain slopes greater than this amount before they break and dissipate energy. A physical picture of the specular points illuminated within a short pulse radar cell advancing at an angle θ with respect to the mean surface normal is shown in (F12.20).

Specular point scatter is readily predictable from geometrical and/or physical optics principles, and has been analyzed by Kodis (1966) and Barrick (1968). Here the theory is extended to include the height of the surface, since the short radar pulse may not illuminate the entire peak-trough region at a given time. As the starting point, we note from elementary geometrical optics principles that the field scattered by N specular points (expressed in terms of the square root of the backscatter cross section) is

$$\sigma_B{}^{1/2} = \sum_{i=1}^{N} \pi^{1/2} g_i{}^{1/2} e^{j2k_o\zeta_i \cos\theta} , \tag{12:38}$$

where g_i is the Gaussian curvature at the i-th specular point, i.e., $g_i = |\rho_{1i}\rho_{2i}|$, with ρ_{1i} and ρ_{2i} as the principal radii of curvature at this point. Also, ζ_i is the height of the i-th specular point above the mean surface, θ is the angle of incidence from the vertical, and $k_o = 2\pi/\lambda$ is the free-space radar wavenumber, λ being the wavelength.

We now square and average the above equation with respect to the phase, φ_{ij}, noting that $\varphi_{ij} = 2k_o(\zeta_i - \zeta_j) \cos\theta$ will be uniformly distributed between zero and 2π as long as the sea waveheight is greater than the radar wavelength. We then rewrite the remaining single summation in integral form as a distribution of specular points versus height, ζ, above the surface and versus Gaussian curvature, g. The average radar cross section per unit surface area per unit height, $\eta^o(\zeta)$, can then be written in terms of the average specular point density, $n(\zeta,g)$ as follows (details are found in Ruck et al, 1971):

$$\eta^o(\zeta) = \pi\int_0^\infty n(\zeta,g)g\,dg , \tag{12:39}$$

where $n(\zeta,g)$ is the average number of specular points within the height interval $\zeta - d\zeta/2$ to $\zeta + d\zeta/2$ and with Gaussian curvatures between $g - dg/2$ and $g + dg/2$. The quantity $\eta^o(\zeta)$ is related to σ^o, the average backscatter cross section per unit area as $\sigma^o = \int_{-\infty}^{\infty} \eta^o(\zeta)\,d\zeta$. Thus a short pulse having a radar resolution cell of width $\Delta\zeta$ will produce, on the average, a radar cross section per unit area of $\eta^o(\zeta)\Delta\zeta$.

The specular point density, n, can readily be determined (almost by inspection) from the work of Barrick (1968) preceding Equation (7) of that paper; one merely includes height, ζ, in the probability densities. The following result—applicable for backscatter—is obtained for the integrand of (12:39):

$$n(\zeta,g)gdg = \pi \sec^4 \theta \; p(\zeta,\zeta_{xsp},\zeta_{ysp},\zeta_{xx},\zeta_{xy},\zeta_{yy})\, d\zeta_{xx} d\zeta_{xy} d\zeta_{yy} \,, \qquad (12:40)$$

where $\zeta_x,\zeta_y,\zeta_{xx},\zeta_{xy},\zeta_{yy}$ are the partial derivatives of the surface height up to second order, ζ_{xsp}, ζ_{ysp} are the surface slopes required at a specular point (these latter slopes are known geometrical quantities). The quantity $p(x_1, \ldots, x_n)$ is the joint probability density function for the random variables $x_1, \ldots, x_n$.

The integration over ζ_{xx}, ζ_{xy}, and ζ_{yy} can now be performed. Furthermore, since the height ζ and the slopes ζ_{xsp}, ζ_{ysp} at any point are uncorrelated (as discussed in 12.1.2), and since we intend to employ Gaussian distributions for the surface height and slopes (also discussed in 12.1.2), we can finally express the scatter per unit height as the product of the height and slope density functions:

$$\eta^0(\zeta) = \pi \sec^4 \theta \; p(\zeta)p(\zeta_{xsp},\zeta_{ysp}) \,, \qquad (12:41)$$

where $p(\zeta)$ is as given in (12:1) and $p(\zeta_x,\zeta_y)$ is given in (12:2). Also, the required total slope at the specular point to be used in (12:2) is $\sqrt{\zeta_{xsp}^2 + \zeta_{ysp}^2} = \tan \theta$.

12.5.2 Application to Satellite Altimeter

We now apply (12:41) to the problem depicted in (F12.21). An altimeter at height H emits a spherical pulse which in turn sweeps past a spherical earth. The spatial pulse width for a backscatter radar is $\Delta\zeta = c\tau/2$, where c is the free space radio wave velocity and τ is the time width of the pulse (compressed, if applicable). As our time reference, we choose $t = 0$ to be the time that the center of the signal, reflected from the uppermost cap of a smooth spherical earth, returns to the receiver. In terms of the angles shown in (F12.21), the height, ζ, to a point at the center of the cell above the mean sea surface can then be written as

or

$$\zeta = \frac{H(1 - \cos\psi) + a(1 - \cos\varphi) - (ct/2)\cos\psi}{\cos\varphi} \,,$$

or

$$\zeta \simeq \frac{H}{2}\psi^2\left(1 + \frac{H}{a}\right) - \frac{ct}{2} \simeq \frac{H}{2}\psi^2 - \frac{ct}{2} \,, \qquad (12:42)$$

where it is assumed that $H \ll a$, and that ψ and φ are small over the scattering region on the sea of significance in the altimeter receiver return.

Several investigators have employed the relationship in (12:42) along with a model for surface scatter, to examine the altimeter radar return. Godbey (1964) and Greenwood et al (1969) assumed quite simple models for the scattering coefficient, and hence obtained a result which was not quantitatively dependent upon ocean waveheight. Miller and Hayne (1971) made a considerable improvement over these efforts by assuming a slightly skewed Gaussian model for $p(\zeta)$ in (12:41), but did not show the remaining slope dependence contained in the specular point model developed here. Hence their radar return, while containing an unspecified multiplicative factor, nonetheless possesses the same pulse shape characteristics as our model.

For the purpose of obtaining a general closed-form containing all of the parameters of interest in the design and analysis of an altimeter experiment, we select simple Gaussian beam and pulse shapes. Thus we define the power gain of the antenna (squared to account for the use of the same antenna twice) as

$$G^2(\psi) = \exp\left\{-(8\ell n2)\psi^2/\Psi_B^2\right\} \,, \qquad (12:43)$$

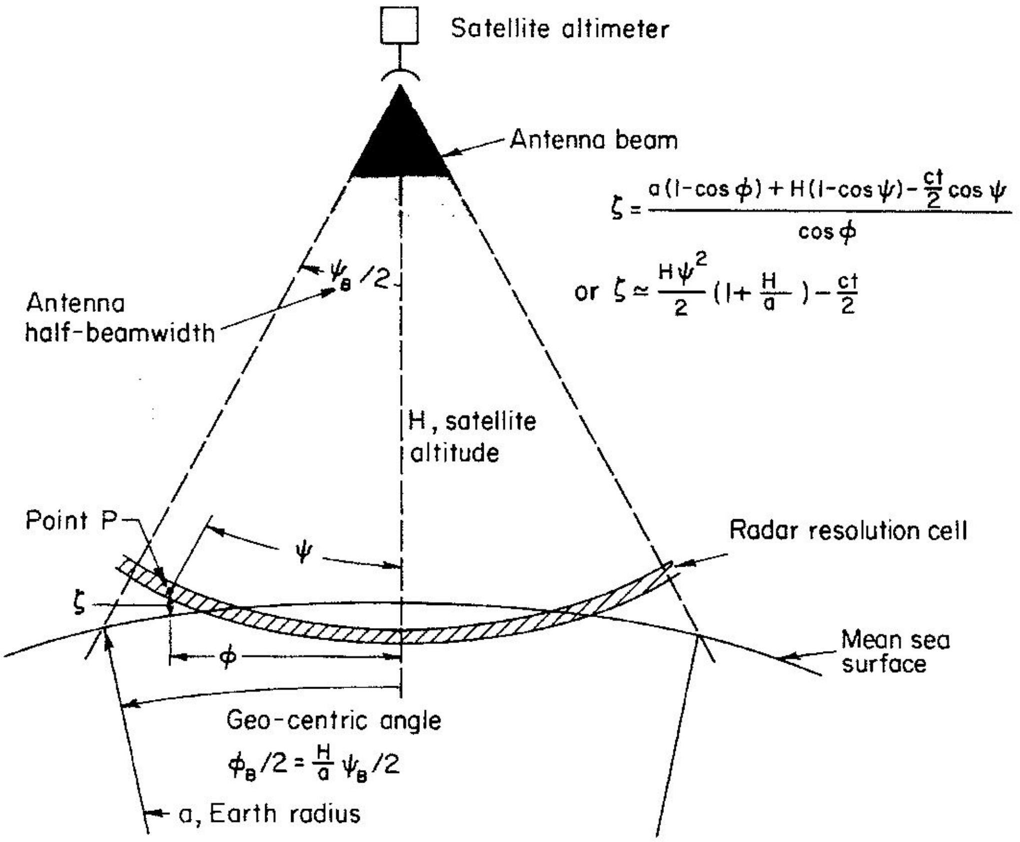

Figure 12.21 *Geometry of satellite altimeter.*

where ψ_B is the one-way half-power antenna beamwidth. Likewise, P(x), defined as the spatial (compressed, if applicable) altimeter signal power pulse, is taken to be

$$P(x) = \exp\left\{-(4\ell n2)t_*^2/\tau^2\right\} = P(ct_*/2)\ , \qquad (12{:}44)$$

where t_* is time with respect to the pulse center, τ is the half-power width of the signal pulse, and the distance x is related to time in a backscatter radar as $x = ct_*/2$.

Now, the product of the average radar cross section and the antenna gain is a function of time as the spherical pulse intercepts the sea near the suborbital point. This produces an average power at the receiver output which is related to $G^2\sigma(t)$ through the radar equation†: $P_R(t) = P_T \frac{\lambda^2}{(4\pi)^3 H^4} G^2\sigma(t)$.

$$G^2\sigma(t) = 2\pi^2 a^2 \int_0^\infty G^2(\psi) p(\zeta_{xsp},\zeta_{ysp}) \sec^4\theta \sin\varphi \times \left[\int_{-\infty}^{\infty} P(\xi - \zeta)p(\xi)\, d\xi\right] d\varphi\ , \qquad (12{:}45)$$

where the Gaussian height and slope distributions, $p(\zeta)$ and $p(\zeta_x,\zeta_y)$ are to be used in integrating (12:45). One can express θ and ψ in terms of φ as follows: $\psi \simeq \frac{a}{H}\varphi$ and $\theta \simeq \psi + \varphi \simeq \frac{a}{H}\varphi$. Then the integrations over ξ and φ

---

† The height factor in the radar range equation is assumed to be constant to first order, because only the echo from the vicinity of the suborbital point is of interest.

can be carried out to obtain:

$$G^2 \sigma(t) = \left(\pi^{3/2} H x_w / s^2\right) \exp[(t_p/t_s)^2 - 2t/t_s] [1 - \Phi(t_p/t_s - t/t_p)] , \qquad (12:46)$$

where $x_w = c\tau/(4\sqrt{\ell n\, 2})$, $t_p = 2\sqrt{x_w^2 + 2h^2}/c$, $t_s = 2H\Psi_e^2/c$, and $1/\Psi_e^2 = (8\, \ell n\, 2)/\Psi_B^2 + 1/s^2$, c being the free-space radio wave velocity. Also, $\Phi(x)$ is the error function of argument x.

The mean-square sea wave height, h^2, and total slope, s^2, result from the use of the Gaussian height and slope distributions given in 12.1.2. For wind-driven fully developed seas, h^2 can be expressed in terms of wind speed through (12:15). The mean-square slope is related to the wind speed through (12:16) and (12:17), or as a simpler model (12.18).

The interpretation of t_p and t_s sheds light on the interaction process. The constant t_p is the equivalent pulse width after stretching by sea waves on a planar mean surface. If the rms height h of the sea waves is greater than the spatial width x_w of the pulse, then the equivalent pulse length after scatter, t_p, is essentially the time of flight between the crests and troughs of the waves. The constant t_s is interpreted as the two-way time of flight difference between the suborbital point and the edge of the effective scattering region illuminated by the advancing spherical pulse. For a narrow antenna beamwidth, Ψ_B, this time becomes small. If the slopes of the specular-scattering waves are smaller than the antenna beamwidth, however, then the width of the scattering region is limited by the lack of specular-scattering sea waves rather than the antenna beamwidth.

A term commonly used in the literature on radar altimeters is the "impulse response" of the surface. This is merely the return from the surface illuminated by an impulse function, $P(x) = \delta(x)$; let us refer to this as $G^2\sigma_I(t)$. To obtain the response of the surface to any other waveform, one need only convolve the surface impulse response with the desired waveform. The impulse response can be obtained very simply from (12:46) by noting that the impulse function $\delta(x)$ can be taken by writing $P(x) = (\pi x_w^2)^{-1/2} \exp -x^2/x_w^2$ in (12:44) and taking the limit of (12:46) as $x_w \rightarrow 0$. We thus obtain

$$G^2 \sigma_I(t) = (\pi H/s^2) \exp\left[(t_p/t_s)^2 - 2t/t_s\right] [1 - \Phi(t_p/t_s - t/t_p)] , \qquad (12:47)$$

where now $t_p = 2\sqrt{2}h/c$.

To provide further insight into the interaction process, and also to serve as a check on the model (12:46), let us consider the limiting situation where the roughness vanishes. First, we allow the rms height, h, to approach zero; we still assume, however, that the rms slope, s, is non-zero, i.e., that there are spatially distributed specular-point scatterers, but with near-zero height deviation from the mean surface. In this limit, the form of (12:46) remains the same, but $t_p = \tau/(2\sqrt{\ell n\, 2})$. Thus the equivalent pulse width, t_p, is not stretched after the interaction because the waves have zero height. Now, as we allow the rms slope, s, to approach zero, this results in $t_s \rightarrow 0$. Then (12:46) simplifies to $G^2\sigma(t) = (\pi H^2) \exp\{-t^2/t_p^2\}$. This merely means that the original Gaussian pulse, represented by the exponential, is reflected from a smooth surface, and hence the entire return comes from the suborbital specular reflection. The factor πH^2 is simply the radar cross section, from geometrical optics considerations, for a spherical surface with radius H. Hence, one obtains the expected result in the limit of vanishing roughness.

12.5.3 Limiting Altimeter Configurations

(a) Pulse-Limited Operation. When the altimeter altitude and/or beamwidth are sufficiently large that $t_s >> t_p$, we have the situation depicted in (F12.22). The return at a given time is obtained from the area in the circular annulus subtended by the pulse. This is referred to as pulse-limited operation. The return in the limit $t_s >> t_p$ may then be obtained from (12:46) as

$$G^2 \sigma_p(t) = \left(\pi^{3/2} H x_w/s^2\right) [1 + \Phi(t/t_p)] \exp(-2t/t_s) . \qquad (12:48)$$

The above equation shows that the return consists of a rapid rise near t = 0, as expressed by the quantity in square brackets, followed by a very gradual exponential decay to zero. In this case, the leading edge of the return contains the desired information about the mean surface position and/or sea state; the

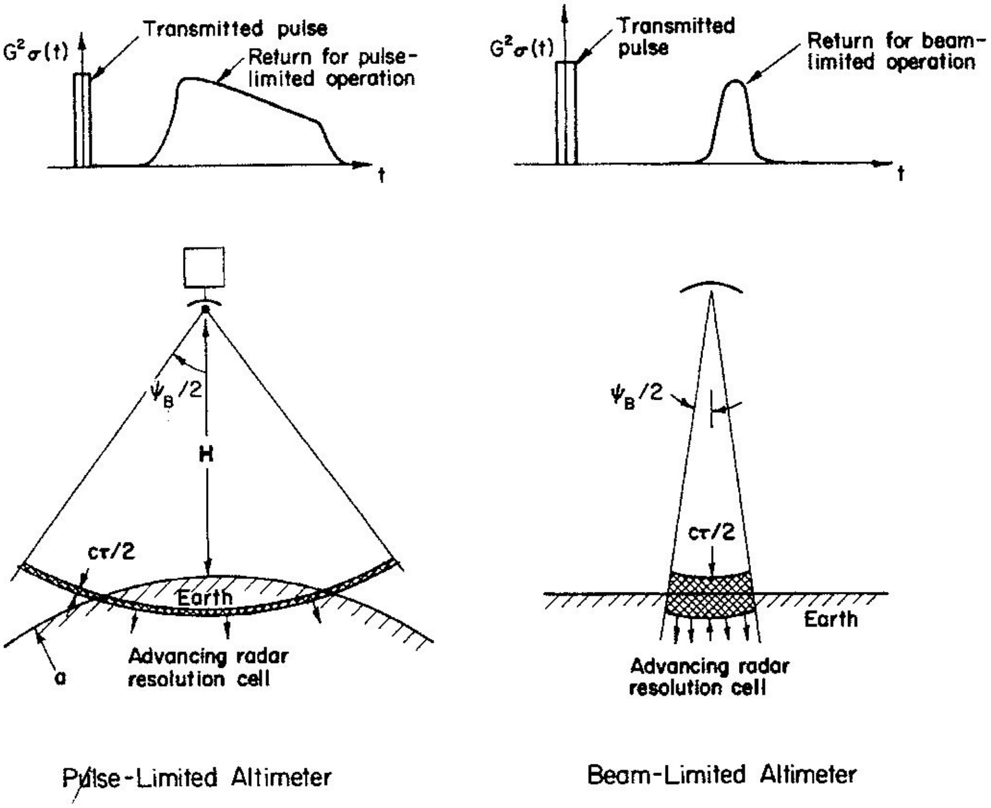

Pulse-Limited Altimeter

Beam-Limited Altimeter

Figure 12.22 *Two modes of altimeter operation and the resulting signals.*

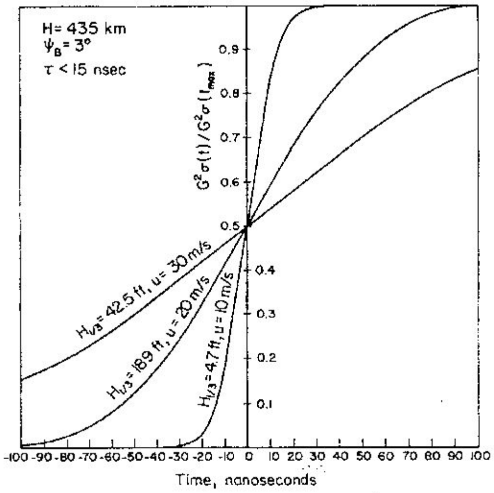

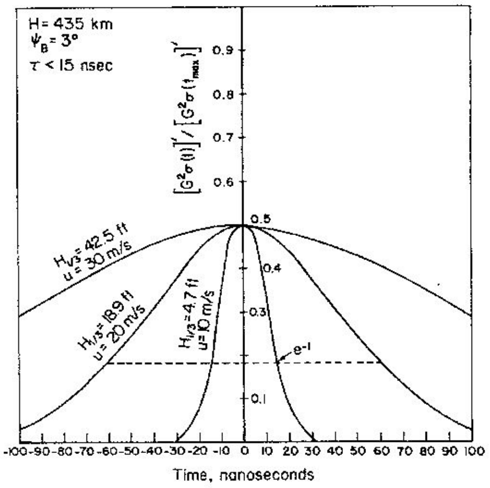

Figure 12.23 *Leading edge of averaged altimeter output versus time for pulse-limited operation.*

Figure 12.24 *Derivative of leading edge of averaged altimeter output versus time for pulse-limited operation.*

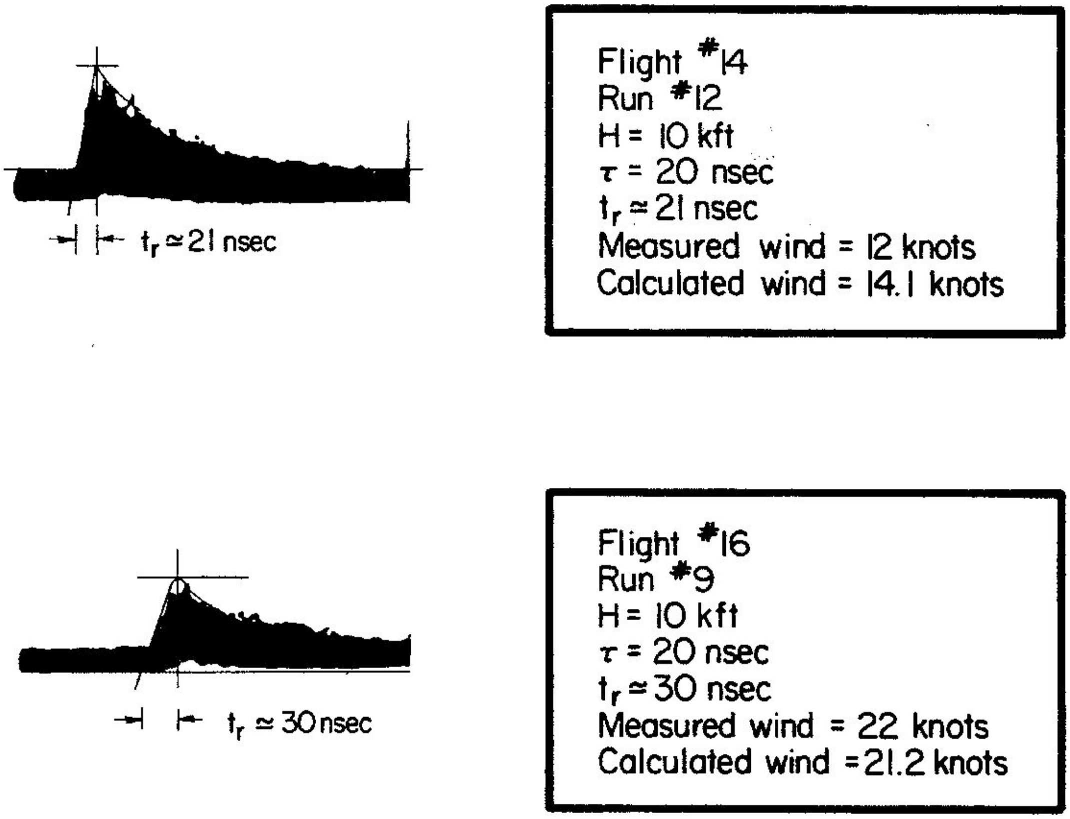

Figure 12.25 *Measured aircraft altimeter responses. Wind speeds inferred from rise times are compared to observed wind speeds.*

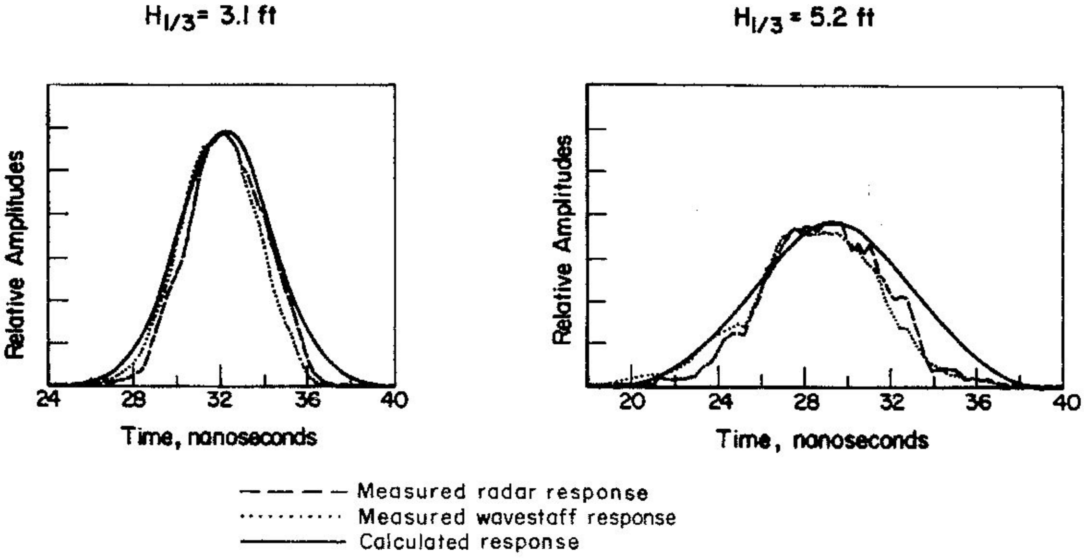

Figure 12.26 *Measured (after Yaplee et al., 1971) altimeter (impulse) responses versus calculated using beam-limited model.*

leading edge (normalized) is proportional to $\frac{1}{2}\left[1 + \Phi(t/t_p)\right]$. Shown in (F12.23) are curves of this leading edge as a function of significant waveheight (related to rms waveheight in 12.1.1). Also shown on these curves are the wind speeds required to fully arouse wind waves to these heights. The parameters chosen are typical of the NASA Skylab satellite altimeter. The figure shows that the mean surface position can be found from the mean return (in the absence of noise) by locating the half-power point on the leading edge.

For sea-state determination, one could determine the rise time of the leading edge. A possibly simpler technique would be to differentiate the mean return near the leading edge, producing a pulse-type signal as shown in (F12.24). This can be obtained from (12:48) as

$$\frac{d}{dt}\left[G^2 \sigma_p(t)\right] \simeq \left[2\pi H x_w/\left(s^2 t_p\right)\right] \exp\left(-t^2/t_p^2\right) . \qquad (12:49)$$

Thus the width of this pulse is directly proportional to the effective pulse width, t_p. If the altimeter pulse width, τ, is kept small with respect to the expected stretching due to roughness (i.e., less than about 15 ns), then the width of this differentiated return is directly proportional to significant (or rms) waveheight. Thus an orbiting altimeter such as this could very simply monitor the significant waveheight of the oceans along its orbital path.

As limited validation of the model, we show results obtained by Raytheon (Ruck et al, 1971) from an aircraft altimeter at 10,000 ft. The pulse width of 20 ns and beamwidth of 5° resulted in a nearly pulse-limited operation. Surface wind speeds were reported as 12 and 22 knots during two of the flights; these are compared in (F12.25) with wind speeds deduced from the rise times, t_r, of the leading edge (assuming wind-driven waves in which waveheight is related to wind speed through (12:15)). The agreement seems quite reasonable.

(b) Beam-Limited Operation. If the antenna beamwidth and/or altimeter height are sufficiently small, then the illumination geometry shown in (F12.22) will result. Here, $t_s \ll t_p$, and the return at any time comes from specular points within a disc of area $\sim\pi H^2 \Psi_e^2/4$ at the suborbital points. In this limit (12:46) can be simplified to obtain:

$$G^2 \sigma_b(t) = \left[\pi H^2 \Psi_e^2/\left(2\sqrt{\ell n 2}\, s^2\right)\right] (\tau/t_p) \exp\left[-(t/t_p)^2\right] . \qquad (12:50)$$

Normally the beamwidth and height requirements are such that a satellite altimeter could almost never be beam-limited; nor are most aircraft altimeters beam-limited. The beam-limited mode of operation does offer a very simple return to interpret, however; the width of the return pulse is directly proportional to the ocean waveheight if the signal pulsewidth, τ, is sufficiently small.

As a comparison with the beam-limited model, we show data measured by Yaplee et al (1971). His measurements were made from a tower with $H = 70$ ft and $\Psi_B \simeq 2°$. His pulse width was 1 ns. We compare in (F12.26) the shape of the curve given by (12:50) with what he has calls his impulse response. He plots the responses measured both by radar and by a wavestaff for two days on which the significant waveheights (measured by the wavestaff) were 3.1 and 5.2 ft; these values of waveheight were used in the curves based on our model. The overall comparison is good, but the figures also illustrate where the Gaussian assumption about the waveheight is weak: both in the echo tails and in the symmetry about the center. These points of departure were mentioned previously in 12.1.2. While these differences are interesting, they should not detract from the fact that the simple Gaussian model is adequate for predicting the mean sea surface position and significant waveheight, so long as accuracies better than about 10 cm are not required.

12.6 References

Barnum, J. R. (1971), Private communication.

Barrick, D. E. (1968), Rough surface scattering based on the specular point theory, IEEE Trans. Ant. Prop. *AP-16*, 449-454.

Barrick, D. E. and W. H. Peake (1968), A review of scattering from surfaces with different roughness scales, Radio Science *3*, 865-868.

Barrick, D. E. (1970), The interaction of HF/VHF radio waves with the sea surface and its implications, Electromagnetics of the Sea, AGARD Conference Proceedings No. 77; also available from Clearinghouse for Federal Scientific and Technical Information, Springfield, Virginia, Accession No. AD-716 305.

Barrick, D. E. and J. A. Grimes (1970), Predicted and measured ground-wave sea clutter spectrum at 6 MHz, presented at Fall USNC/URSI Meeting, September 15-17, Columbus, Ohio.

Barrick, D. E. (1971 a), Theory of HF/VHF propagation across the rough sea, Parts I and II, Radio Science *6,* 517-533.

Barrick, D. E. (1971 b), Dependence of second-order sidebands in HF sea echo upon sea state, pp. 194-197, 1971 G-AP International Symposium Digest, September 21-24, Los Angeles, California.

Barrick, D. E. (1972), First-order theory and analysis of MF/HF/VHF scatter from the sea, IEEE Trans. Ant. Prop. *AP-20,* 2-10.

Bascom, W., 1964: *Waves and Beaches.* Anchor Books, Doubleday & Co., Inc., Garden City, New York.

Cox, C. S. and W. H. Munk (1954), Statistics of the sea derived from sun glitter, Jour. Marine Res. *13,* 198-227.

Crombie, D. D. (1955), Doppler spectrum of sea echo at 13.56 Mc/s, Nature *175,* 681-682.

Crombie, D. D., J. M. Watts and W. M. Beery (1970), Spectral characteristics of HF ground wave signals backscattered from the sea, Electromagnetics of the Sea, AGARD Conference Proceedings No. 77; also available from Clearinghouse for Federal Scientific and Technical Information, Springfield, Virginia, Accession No. AD-716 305.

Crombie, D. D., 1971: Backscatter of HF radio waves from the sea, pp. 131-162 of J. R. Wait, ed. *Electromagnetic Probing in Geophysics,* The Golem Press, Boulder, Colorado.

Davies, H. (1954), The reflection of electromagnetic waves from a rough surface, Proc. IEE, Part III *101,* 209-214; discussion on above paper Proc. IEE, Part III *102,* 148.

Godbey, T. W. (1964), Oceanographic satellite radar altimeter and wind sea sensor, pp. 21-26 of G. C. Ewing, ed. Oceanography in Space, Proceedings of Conference, Woods Hole Oceanographic Institution, Reference No. 65-10, August 24.

Greenwood, J. A., A. Nathan, G. Neumann, W. J. Pierson, F. C. Jackson and T. E. Pease, 1969: Radar altimetry from a spacecraft and its potential applications to geodesy, pp. 59-80 *Remote Sensing of the Environment,* Vol. 1, American Elsevier Publishing Co., Inc., New York.

Guinard, N. W. and J. C. Daley (1970), An experimental study of a sea clutter model, Proc. IEEE *58,* 543-550.

Hasselmann, K. (1971), Determination of ocean wave spectra from Doppler radio return from the sea surface, Nature Physical Science *229,* 16-17.

Kinsman, B., 1965: *Wind Waves.* Prentice-Hall, Inc., Englewood Cliffs, New Jersey.

Kodis, R. D. (1966), A note on the theory of scattering from an irregular surface, IEEE Trans. Ant. Prop. *AP-14,* 77-82.

MacKay, J. H. (1959), On the Gaussian nature of ocean waves, Engineering Experiment Station, Georgia Institute of Technology, Atlanta, Georgia, Internal Technical No. 8.

Miles, J. W. (1962), On the generation of surface waves by shear flows, Part 4, J. Fluid Mech. *13*, 433-448.

Miller, L. S. and G. S. Hayne (1971), System study of the geodetic altimeter concept, Research Triangle Institute, Research Triangle Park, North Carolina, Final Report, Contract No. NAS6-1829 (March 1971), Unclassified.

Moskowitz, L. (1964), Estimates of the power spectrums of fully developed seas for wind speeds of 20 to 40 knots, J. Geophys. Res. *69*, 5161-5179.

Munk, W. H. and W. A. Nierenberg (1969), High frequency radar sea return and the Phillips saturation constant, Nature *224*, 1285.

Nathanson, F. E. (1971), Radar pulse compression and high resolution sea reflectivity, Proceedings of Joint NOAA/NASA/NAVY Conference on Sea Surface Topography from Space, October 6-8, Key Biscayne, Florida.

Nierenberg, W. A. and W. H. Munk (1969), Sea spectra and radar scattering, 1969 JASON Summer Study Working Paper, Boulder, Colorado.

Peake, W. H. (1959), Theory of radar return from terrain, Part 1, IRE Int. Conv. Record 7, 27-41.

Peterson, A. M., C. C. Teague and G. L. Tyler (1970), Bistatic radar observation of long-period directional ocean-wave spectra with LORAN A, Science *170*, 158-161.

Phillips, O. M., 1966: *Dynamics of the Upper Ocean.* Cambridge University Press, London, pp. 109-119.

Rice, S. O., 1951: Reflection of electromagnetic waves from slightly rough surfaces, pp. 351-378 of M. Kline, ed. *Theory of Electromagnetic Waves,* Interscience Publishers, New York.

Ruck, G. T., D. E. Barrick and T. Kaliszewski (1971), Bistatic radar sea state monitoring, Battelle, Columbus Laboratories, Columbus, Ohio, Technical Report, Contract NAS6-2006 (December, 1971), Unclassified.

Stewart, R. H. (1971), Higher order scattering of radio waves from the sea, pp. 190-193, 1971 G-AP International Symposium Digest, September 21-24, Los Angeles, California.

Teague, C. C. (1971), High-frequency resonant scattering techniques for observation of directional ocean-wave spectra, Stanford University, Stanford, California, Technical Report No. SU-SEL-71-039, Contract N00014-69-A-0200-6012, Unclassified; also available as Ph.D. dissertation under same title, University Microfilms, Ann Arbor, Michigan.

Tveten, L. H. (1967), Ionospherically propagated sea scatter, Science *157*, 1302-1304.

Valenzuela, G. R. (1968), Scattering of electromagnetic waves from a tilted slightly rough surface, Radio Science *3*, 1057-1066.

Wait, J. R. (1966), Theory of HF ground wave backscatter from sea waves, J. Geophys. Res. *71*, 4839-4842.

Ward, J. F. (1969), Power spectra from ocean movements measured remotely by ionospheric radio backscatter, Nature *223*, 1325-1330.

Wright, J. W. (1968), A new model for sea clutter, IEEE Trans. Ant. Prop. *AP-16*, 217-223.

Yaplee, B. S., A. Shapiro, D. L. Hammond, B. D. Au and E. A. Uliana (1971), Nanosecond radar observations of the ocean surface from a stable platform, IEEE Trans. Geoscience Electronics, GE-9, 170-174.

Zamarayev, B. D. and A. I. Kalmykov (1969), On the possibility of determining the spatial structure of an agitated ocean surface by means of radar, Izvestia USSR Academy of Sciences – Atmospheric and Oceanic Physics *5*, 64-66.

List of Symbols

a	(radio) radius of earth ($\simeq$4/3 times actual earth radius)
a	spatial wavenumber of fundamental in Fourier expansion of (ocean) surface waveheight ($=2\pi/L_f$)
B	Phillips ocean waveheight spectrum saturation constant ($\simeq$0.005)
c	free-space radio wave velocity ($\simeq 3 \times 10^8$ m/s)
d	half the distance between transmitter and receiver in bistatic radar
E_o	electric field intensity incident on scattering patch
F_T, F_R	Norton attenuation factors for near surface propagation between scattering patch and transmitter, receiver.
f	temporal frequency in cycles per second
f_o	radio carrier frequency
f_b, f_a	carrier frequencies in two-frequency sensor
f_D	Doppler shift from carrier ($= f - f_o$)
f_N	normalized Doppler shift
G_T, G_R	free-space gains of transmitter and receiver antennas
g	acceleration of gravity ($\simeq 9.81 \mathrm{m/s^2}$)
g	Gaussian curvature of point on surface ($= \lvert\rho_1 \rho_2\rvert$)
H	height of radar altimeter
$H_{1/3}$	significant (ocean) waveheight, crest-to-trough
h	rms (ocean) waveheight with respect to mean surface
i	imaginary number symbol ($=\sqrt{-1}$)
k_o	radar wavenumber ($= 2\pi/\lambda$)
k,m,n	summation indices, assuming integer values
L	spatial period of ocean wave
L_{co}	cutoff (spatial) wavelength of Phillips ocean waveheight spectrum
L_f	spatial wavelength of fundamental in Fourier expansion of (ocean) surface waveheight.
$n(\zeta,g)$	density of specular points per unit area versus height and Gaussian curvature
P_b, P_a	powers received at two frequencies, f_b and f_a
$P(m,n,k)$	Fourier coefficient of expansion of ocean surface height in terms of x, y, t
x, y, t	
P_R	average received power at receiver
$P_R(\omega)$	average received power spectral density at receiver
P_T	average transmitted power
$P(x)$	effective spatial (power) pulse of radar altimeter
$P(x_1, \ldots x_n)$	joint probability density function of n random variables $x_1, \ldots, x_n$
R_o	distance from antenna to scattering patch in backscatter radar
R_T, R_R	ranges (distances) from scattering patch to transmitter and receiver
S	normalized time delay in bistatic radar ($= t/t_d$)
$S(\kappa_x, \kappa_y)$	spatial ocean waveheight spectrum
$S(\kappa_x, \nu_y, \omega)$	spatial-temporal ocean waveheight spectrum

$S(\omega)$	temporal ocean waveheight spectrum
s	rms total (ocean) waveslope $\left(=\left[\langle\zeta_x^2+\zeta_y^2\rangle\right]^{1/2}\right)$
$\mathrm{sgn}(p)$	symbol taking value ±1 depending on whether argument p is ±
T	temporal period of ocean wave
T_f	temporal wavelength of fundamental in Fourier expansion of (ocean) surface waveheight
t	time delay of radar echo
t_d	time delay for direct pulse between transmitter and receiver in bistatic radar
t_r	rise time in altimeter radar return
t_s, t_p	time constants (parameters) appearing in altimeter return model
U, V	normalized ocean spatial wavenumbers $(= \kappa_x/2k_o, \kappa_y/2k_o)$
u	wind speed
v	phase velocity of ocean wave
v_s	satellite velocity
v_{sh}	ship speed
$W(\kappa_x, \kappa_y, \omega)$	alternate (radio scatter) definition of spatial-temporal ocean waveheight spectrum $(= 2^3 S(\kappa_x, \kappa_y, \omega))$
$W_{SL}(\kappa_x)$	ocean waveslope spatial spectrum for longer gravity waves
w	temporal wavenumber of fundamental in Fourier expansion of (ocean) surface waveheight $(= 2\pi/T_f)$
$\langle x \rangle$	ensemble average of random variable x
x_w	effective spatial altimeter pulse with after stretching by ocean waves
Z_o	wave impedance of free space $(\simeq 120\pi$ ohms)
α	grazing angle
Γ_{EM}	coupling factor for electromagnetic second-order sea scatter terms
Γ_H	coupling factor for hydrodynamic second-order sea scatter terms
Γ_T	total coupling factor appearing in integrand for second-order sea scatter
Δ	normalized average impedance of sea surface; also, symbol denoting an increment, i.e., ΔR – increment of range
$\delta(p)$	Dirac impulse function of argument p
ζ	height of ocean surface above mean plane
ζ_x, ζ_y	directional slopes of ocean surface in (orthogonal) x and y directions $\left(= \frac{\partial\zeta}{\partial x}, \frac{\partial\zeta}{\partial y}\right)$
η	radian Doppler shift from carrier $(= \omega - \omega_o)$
$\eta^0(\zeta)$	average backscatter cross section per unit area per height increment
θ	angle between mean normal to surface and incidence or scatter direction
θ	variable in elliptical coordinate system
θ_i	angle of incident radar wave from vertical
θ_s	angle of scattered radar wave from vertical
κ	spatial wavenumber of ocean wave $(= 2\pi/L)$
κ_c	spatial wavenumber of ocean waves at threshold between gravity and capillary region $(= 3.8\ \mathrm{cm}^{-1})$
κ_{co}	cutoff (spatial) wavenumber of Phillips ocean waveheight spectrum
κ_x, κ_y	spatial (ocean) height wavenumbers in (orthogonal) x and y directions
λ	radar wavelength
μ	variable in elliptical coordinate systems
ρ_1, ρ_2	principal radii of curvature at point on surface
σ^0	average scattering cross section of sea per unit area
$\sigma(\omega)$	average scattering cross section of sea per unit area per rad/s bandwidth
τ	radar temporal pulse width

$\Phi(x)$	error function of argument x
φ	azimuthal angle in bistatic radar near surface between incidence and scatter plane ($\varphi = 180°$ for backscatter); also, in radar altimeter, angle at earth center between altimeter and surface scattering patch
φ_s	azimuthal angle of scattered radar wave from incidence plane
Ψ_B	half-power beamwidth of radar altimeter antenna
ψ	angle of radar altimeter between vertical and scattering point on earth
ω	temporal wavenumber of ocean wave ($= 2\pi/T$)
ω_o	radian wavenumber of radio carrier frequency
ω_B	radian Doppler shift for near-grazing backscatter ($=\sqrt{2k_o g}$)
ω_{dm}	maximum satellite-induced (radian) Doppler shift
ω_m	maximum ship-induced (radian) Doppler shift
ω_s	radian Doppler shift from sides of ellipse in bistatic radar